POLITECNICO DI MILANO
DIPARTIMENTO DI SCIENZE E TECNOLOGIE AEROSPAZIALI
LAUREA MAGISTRALE IN INGEGNERIA AERONAUTICA

ACTIVE TURBULENCE CONTROL THROUGH WALL DEFORMATION IN CHANNEL FLOW

MSc Thesis of:
Alessandro Testa

Matricola:
905142

Supervisor:
Prof. Quadrio Maurizio

Tutor:
Ing. Banchetti Jacopo

Year – 2019/2020

Acknowledgement

I would like to express my deepest gratitude to my supervisor, professor Maurizio Quadrio, for giving me the opportunity to perform this study and for sharing his experience with me. A special thank to Jacopo Banchetti for giving me valuable advice and for pushing me to do better and better.
Il mio primo immenso ringraziamento va ai miei genitori ed ai miei nonni, senza i quali questo lavoro non sarebbe mai stato possibile. Un grazie per avermi accudito, cresciuto e reso la persona che sono; grazie per avermi sempre supportato nelle scelte, anche quelle più folli, per avermi incoraggiato e insegnato che con l'impegno, la dedizione e la passione si possono raggiungere dei risultati che, a volte, vanno oltre le nostre capacità.
Un grazie speciale a Jessica, che da quando ci siamo conosciuti tre anni fa mi è sempre stata accanto, dandomi amore, sopportando le mie continue lamentele e credendo alle mie idee malsane.
Un grazie a Moreno per essere un vero amico, disponibile nel momento del bisogno, con il quale ho vissuto un numero incalcolabile di esperienze. Un grazie di cuore ad Andre, per avermi tirato fuori dai pasticci in più occasioni e grazie per aver reso, insieme ad Edo, le lunghe giornate al poli assai meno grigie. Grazie a Lele e Giada per avermi praticamente adottato e dato, insieme a mille saggi consigli di vita, un fratellino: Lellino. Grazie ad Alan per essere stato il mio compagno di banco per quasi cinque anni e grazie a Ludo, Ari e Lucri per aver condiviso con me, in tutto questo tempo, un buon numero di vasche in piscina rendendole un po' meno noiose.
Un grazie a tutti i miei amici più stretti, coloro che posso non vedere magari per molto tempo, ma che posso ogni volta ritrovare scoprendo che non sembra passato nemmeno un giorno.

Grazie a tutti,

July 11, 2020

Alessandro

Sommario

QUESTO studio è volto ad investigare, mediante la simulazione numerica diretta, uno schema di controllo attivo, ispirato al controllo opposto (opposition control) [6], ma che, applicato alla geometria del canale piano turbolento, sia realizzato attraverso la deformazione delle pareti del canale stesso. Lo scopo ultimo è quello di ottenere un risparmio netto di potenza immessa per sostenere il flusso mantenendo la portata costante. Lo schema di controllo sviluppato è retro-azionato, lineare ad azione proporzionale-integrale-differenziale (PID), nel quale il punto di controllo può essere posizionato, eventualmente, a monte del punto di attuazione. In questo lavoro le direzioni x e y rappresentano rispettivamente la direzione longitudinale e trasversale al flusso mentre, la direzione z è perpendicolare alla parete del canale, nella sua posizione di riferimento. La velocità di deformazione delle pareti del canale è data da tre contributi: il primo è proporzionale alla velocità del fluido normale alla parete nella sua condizione di riferimento; il secondo è proporzionale alla differenza tra l'attuale posizione della parete e la sua posizione di riferimento; infine, il terzo è proporzionale all'accelerazione della parete. La formula che regola la velocità di deformazione della parete nel punto (x, y) al tempo t può essere dunque scritta come:

$$w^w_{(x,y,t)} = - K_p \cdot w_{(x-\delta x,y,z_c,t)} - K_i \cdot \left(z^w_{(x,y,t)} - z^{w,ref} \right) + \\ - K_d \cdot \left(w^w_{(x,y,t)} - w^w_{(x,y,t-\Delta t)} \right) / \Delta t \qquad (1)$$

nella quale l'apice w è usato per indicare valori di parete. Inoltre si vuole precisare che z_c è la coordinata del punto di controllo e δx realizza la possibilità di spostare il punto di controllo a monte o a valle del punto di attuazione. Come detto lo strumento di calcolo utilizzato è quello della simulazione numerica diretta (DNS), nella quale le equazioni di Navier-Stokes sono risolte numericamente senza l'utilizzo di alcun modello di turbolenza. In questo lavoro il flusso è considerato instazionario, viscoso e incomprimibile. Il codice di calcolo DNS, introdotto da Luchini [29], risolve le equazioni di Navier-Stokes in variabili primitive all'interno di una griglia di calcolo Cartesiana sfalsata (staggered Cartesian grid). Le derivate in ciascuna direzione sono approssimate utilizzando un metodo alle differenze finite del secondo ordine. L'avanzamento temporale è,

invece, completato utilizzando un metodo Runge-Kutta a tre passi, del terzo ordine di accuratezza. La forma complessa della parete, dovuta al movimento caotico del flusso turbolento che si ripercuote, attraverso la legge di controllo, sulla velocità della parete stessa, è superata grazie all'utilizzo di un metodo a confini immersi (immersed boundary). Quest'ultimo rende la generazione della griglia di calcolo banale ed eseguita una volta per tutte all'inizio di ogni simulazione. Si tiene a precisare che, grazie all'ottima efficienza del codice di calcolo, tutte le simulazioni sono state condotte mediante un desktop computer, appositamente assemblato per rispondere a specifiche esigenze. Ciò mette in luce che non sono sempre necessarie eccezionali potenze di calcolo, nemmeno per alcuni calcoli DNS seppure preliminari e a basso numero di Reynolds.

Il lavoro è stato suddiviso in due parti: nella prima si è utilizzato un dominio di calcolo che consentisse di eseguire un grande numero di simulazioni in tempi relativamente brevi; successivamente, nella seconda parte, si è adottato un dominio di calcolo tale da ottenere statistiche in indubbio modo affidabili. La differenza nel tasso di risparmio netto di potenza calcolato eseguendo due simulazioni, con gli stessi parametri, ma utilizzando i due diversi domini di calcolo, è risultata all'incirca del 1%.

Nella prima parte del lavoro sono state eseguite più di 80 simulazioni a $Re_\tau = 180$ analizzando la variazione del rateo di risparmio netto di potenza; ciò è stato fatto rispetto a vari valori del termine proporzionale e di quello integrale, e in funzione della posizione longitudinale, determinata dal punto di attuazione, e verticale del punto di controllo. In aggiunta sono stati esaminati un paio di casi con l'utilizzo di un controllo selettivo in grado di contro-agire i movimenti del fluido verso la parete (sweep) o, viceversa, i movimenti del fluido dalla parete (ejection). In generale si è dimostrato che si ottiene un maggiore tasso di risparmio netto di potenza aumentando il valore del coefficiente del termine proporzionale K_p. Tuttavia, se tale valore viene aumentato fino a superare 1.3, lo schema di controllo diventa instabile e le simulazioni esplodono; è stato osservato che l'introduzione di un fattore di smorzamento ($K_d \approx 10^{-3}$) elimina completamente le oscillazioni consentendo di aumentare il coefficiente proporzionale oltre la soglia di 1.3.
L'introduzione di un termine integrale, regolato in ampiezza dal coefficiente K_i, è stata necessaria per ridurre l'eccessiva deformazione delle pareti del canale altrimenti prodotta. Si è ottenuto un tasso di risparmio netto di potenza per un intervallo relativamente ampio di valori di K_i; il valore più opportuno dipende sia dalla scelta del coefficiente proporzionale K_p sia dalla posizione del piano di rilevazione z_c.
Diversamente da quanto mostrato in diversi articoli trattanti il controllo opposto classico, l'efficacia dello schema di controllo sviluppato nel corso di questo lavoro risulta essere molto meno sensibile alla posizione del piano di rilevamento. È stato infatti ottenuto un risparmio netto di potenza per valori di z_c molto differenti; neppure quando il piano di rilevamento è stato posto a 40 unità di parete, dalla posizione media della parete del canale, si è riscontrato un aumento della potenza totale necessaria. Si ricorda che nel controllo opposto si ottiene un aumento di resistenza, anziché una riduzione, già quando il piano di rilevamento è posto a 23 unità di parete.
Posizionando il punto di rilevamento a monte del punto di attuazione ($\delta x \approx 0.1$) si ottiene un leggero miglioramento del tasso di risparmio netto di potenza ottenibile, come avviene per il controllo opposto classico.
Il controllo selettivo ha, invece, mostrato un risultato inaspettato: il controllo dei soli movimenti del fluido verso la parete fornisce un risparmio netto di potenza, analogo

a quello ottenuto controllando i soli movimenti del fluido dalla parete verso il centro del canale. Inoltre tale risparmio è inferiore a quello ottenuto controllando entrambi i movimenti del fluido. Al contrario ci si aspettava che il controllo dei soli movimenti del fluido verso la parete fosse più efficace del solo controllo dei movimenti di fluido dalla parete. Tale risultato può tuttavia dipendere dalla specifica configurazione di parametri utilizzata in questa particolare analisi.
In generale un risparmio netto di potenza è stato ottenuto per molteplici combinazioni differenti di parametri, il che indica un'ottima efficienza e stabilità dello schema di controllo; oltretutto, per alcuni gruppi di parametri, è stata ottenuta una significativa riduzione della potenza totale immessa ($\approx 20\%$).

In seguito sono state analizzate con maggiore dettaglio due simulazioni (sempre a $Re_\tau = 180$), tra quelle che avevano dato il più alto risparmio netto di potenza, per validare i risultati precedentemente ottenuti.
Da queste simulazioni è apparso che il contributo di pressione alla potenza totale immessa è trascurabile; ciò implica che la resistenza dovuta alla forma della parete sia anch'essa trascurabile. Tuttavia la forma altamente irregolare delle pareti del canale potrebbe causare un aumento delle fluttuazioni della velocità destabilizzando, in questo modo, il flusso.
Il contributo di potenza necessario per attuare il movimento delle pareti è apparso significativo e rappresenta circa il 10% della potenza totale immessa. Ciò implica che, se confrontato con il controllo opposto classico, questo schema di controllo sarebbe in grado di fornire la stessa riduzione di resistenza; tuttavia il controllo opposto classico risulta essere più efficiente, richiedendo una minor potenza necessaria a realizzare il controllo.
L'intercetta della legge logaritmica risulta aumentata similmente a quanto avviene in diversi flussi soggetti a riduzione di resistenza.
È stato inoltre dimostrato che lo schema di controllo modifica profondamente il comportamento del flusso; ciò avviene nella regione più vicina a parete mentre, viceversa, ha un effetto minimo o nullo nella regione centrale del canale. Le fluttuazioni di velocità e lo sforzo di Reynolds, così come la produzione di energia cinetica turbolenta, sono ridotte rispetto al canale non controllato. In modo differente la dissipazione di energia cinetica turbolenta è apparsa influenzata in modo minore dal movimento delle pareti del canale rispetto alla produzione.
In più si è osservato uno spostamento delle statistiche delle quantità turbolente verso il centro del canale.

Sebbene questo lavoro abbia ottenuto alcuni risultati degni di nota in termini di potenza netta risparmiata per sostenere il flusso, deve comunque essere inteso come un punto di partenza, eppure valido. L'idea che sta alla base della legge di controllo sviluppata, infatti, promette di offrire risultati ancor più vantaggiosi rispetto a quelli in seguito riportati. Tale lavoro può inoltre fornire diversi spunti per comprendere con maggiore dettaglio l'influenza che il movimento di una superficie solida ha sul flusso che vi scorre.

Abstract

THIS study is aimed to investigate a linear proportional-integral-differential (PID) feedback control using, eventually, an upstream sensor with the purpose of a net power saving in a turbulent channel flow at $Re_\tau \simeq 180$. Direct numerical simulations are performed analyzing the variation of the net power saving rate respect to the proportional and integral terms, and the streamwise and z-coordinate of the sensor location. Furthermore, selective control, capable of counteracting only sweep or only ejection events, is briefly examined. The resulting complexity of the wall shape is overcome with the use of an immersed boundary method, which makes the mesh generation trivial and done once at the beginning of each simulation. A net power saving rate is achieved for many different combinations of parameters indicating good effectiveness and stability of the control scheme; moreover, remarkable power saving is obtained under some sets of parameters ($\approx 20\%$). The control profoundly modifies the near-wall flow behavior whereas, on the contrary, it has minimal effect in the outer region; the velocity fluctuations and the Reynolds shear stress, as well as the production of turbulent kinetic energy, are reduced. Besides, an outward shift of turbulence statistics in the controlled flow is observed.

Keywords: immersed boundary method; channel flow; opposition control; skin-friction drag reduction; upstream sensor

Contents

List of Figures

List of Tables

CHAPTER 1

Introduction

Due to the impact of the oil crisis in the 1970s and the increasing attention to environmental sustainability issues, in the past decades, a great effort has been spent in developing and investigating the most varied flow control strategies to achieve drag reduction. Furthermore, given that most of the fluid flows that occur in real-world applications are known to be turbulent, the benefits of controlling turbulence production in the near-wall region, using an effective control strategy, can lead to relevant power savings.

It has been consistently demonstrated that, close to the wall, turbulence is sustained by a cyclic and spatially organized process [13], [18]. This process has some definite characteristics: high-speed fluid is pushed toward the wall, whereas low-speed fluid is ejected from the wall by the so-called quasi-streamwise vortices, resulting in elongated regions of spanwise alternating high and low-speed fluid [17]. These coherent structures in the near-wall region ($0 < z^+ < 100$, in which z^+ is the dimensionless distance from the wall surface in viscous units) play a crucial role in turbulence production; in particular, it has been proven that substantially all turbulence production takes place during intermittent bursting events [21], which consist of the lift-up, oscillation, and, finally, breakup of the low-speed streaks [38], [1]. Even sweep events, which push high-speed fluid toward the wall, are known to be a primary source in turbulence production since they create strong velocity gradients in the proximity of the wall, resulting in zones of high skin-friction. For a detailed and comprehensive knowledge on the near-wall region consult [35].

To attenuate the effect of turbulent motion leading to a net power saving, in the past thirty years many drag reduction techniques, both passive and active, have been investigated. Passive strategies do not require any external energy supply and work interacting with the wall cycle generally through some kind of beneficial roughness. These techniques are proven to give $7 - 8\%$ drag reduction at $Re_\tau \simeq 180$ [42], [5],

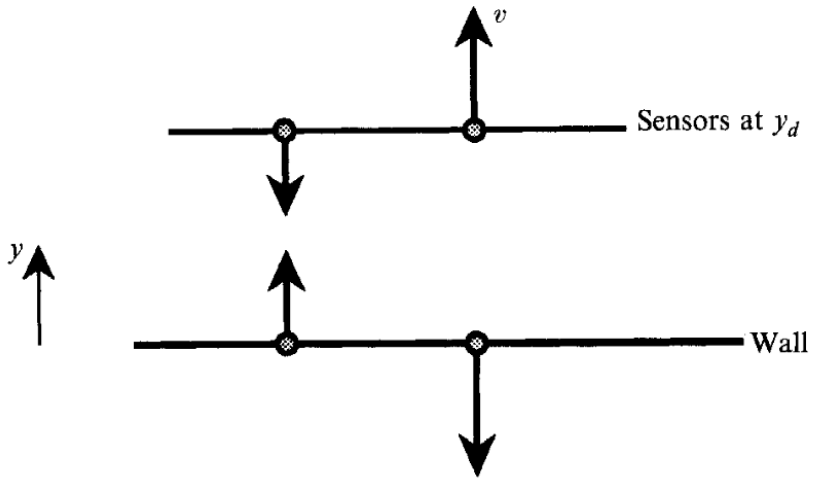

Figure 1.1: *Schematic diagram of out-of-phase v-control from [6].*

but maintenance places a tough barrier on their applicability. Active control strategies require an additional power source as they work by exploiting wall motion or deformation to weaken turbulence near the wall. However, also thanks to the development of new technologies, such as MEMS (micro-electro-mechanical systems) [20], these techniques could be much more effective when compared to those passive strategies.

Among active feedback control strategies, opposition control, realized through suction and blowing on the wall, has been deeply investigated since 1994. Choi, Moin, and Kim firstly proposed the opposition control to counteract the near-wall coherent structures [6]; in their study, blowing and suction was opposite to the wall-normal velocity at a given detection plane, as illustrated in figure 1.1. Later, Chung and Talha conducted a study varying the sensing plane location and the amplitude of suction and blowing [7] and demonstrated that the optimal position of the detection plane depends on the strength of the control. Furthermore, opposition control using upstream sensors was also investigated by Lee [27]. The dependence of the efficiency of the opposition control to higher Reynolds number was investigated by Iwamoto, Suzuki, and Kasagi [16] in 2002, and later in 2007 by Pamiés et al. [34], instead. Since the concept of placing sensors very close to the wall is practically difficult, if not impossible, control methods with sensors at the wall were introduced [26], [28]. Son, Jeon, and Choi applied proportional, proportional-integral and proportional-differential feedback controls, realized through suction and blowing, to flow over a circular cylinder for suppression of vortex shedding in the wake [41]; Kim and Choi examined a proportional-integral feedback control to a turbulent channel flow [22] instead. Even if important drag reduction rates (25-30% at $Re_\tau \simeq 180$) have been achieved some concepts of opposition control seem to be hardly feasible for implementations.

Many other studies explored the benefits of predetermined active wall motion to suppress or counteract the near-wall coherent structures. Quadrio and Ricco analyzed the advantages of lateral sinusoidal oscillations of the channel walls [37]. Streamwise-traveling waves of wall deformation obtained impressive drag reduction rates and even relaminarization of the entire flow under some particular sets of parameters [31]. Nevertheless, these feedforward control methods are expected to be less effective if compared

to feedback ones.

However, to date only few researches dealt with active feedback control applied to deformable walls [19], [9]. Since one of the most practical control strategies for drag reduction is active walls motion and PID controllers are readily available on the market, this work, inspired by the classical opposition control, wants to investigate what may be accomplished through wall deformation given by active feedback control based on a linear proportional-integral-differential controller. This study should be understood as a first firm point: despite positive results have been obtained in terms of net power saved and known values of drag reduction, achieved through similar control techniques, have been improved about few percentage points, this strategy, consisting in wall deformation given by a feedback control law, promises to give even better drag reduction rates or even flow relaminarization. Furthermore, this study could be a starting point to understand the effects of the wall motion on the near-wall coherent structures.

Direct numerical simulations (DNS) can provide helpful results on what may be accomplished through flow control methods. Unfortunately the domain dimensions and complexity and the Reynolds number must be limited as a consequence of the extreme computational cost. Thanks to Paolo Luchini and his achievements in developing an efficient immersed boundary method (IBM) the limitation to simple geometry could be easily overcome [29]. Moreover, the increased computational power available nowadays even in desktop computers gives extraordinary research possibilities: in fact all the simulations presented in the following pages have been performed on an ad-hoc assembled desktop computer. This latter fact is of great importance since it highlights that not always extreme computational powers are necessary for the direct numerical simulation. In this study an IBM solver is used for the direct numerical simulation of a fully developed channel flow at $Re_\tau = 180$. Mesh resolution and domain dimensions are such as to resolve the smallest scales of motion and to include the largest eddies in the flow.

This paper is organized as follows. In chapter two are presented a detailed explanation of the numerical method used, the control law developed, and the data related to the computational domain; a discussion about the total dissipation concludes the chapter. Then, chapter three reports a parametric analysis of several numerical experiments with backward wall motion. In chapter four are deepen a reference plane channel and two simulations with active control. Finally, a summary and possible future developments conclude this work.

CHAPTER 2

A fundamental background

Both the numerical method and the programming language used in this work were conceived and developed by Paolo Luchini [29]; then, the code has been recently used to investigate the effects of skin-friction drag reduction in a turbulent flow over a curved wall [3]. Considering that the code and the programming language were thought and built unitedly, the performances are high as well as the parallel scaling features. The code has already been tested and validated with existing data in the literature using both immersed non-moving and moving (peristaltic wall motion) boundaries [40]. Further analysis has been repeated in the course of this work using non-moving and moving wall and investigating many different flow control strategies; particular attention has been paid to peristaltic wall motion and suction and blowing on the wall in addition to the control scheme developed in this work. Know results have been replicated indicating the correct functioning of the numerical code even after the introduction of the modifications needed for the implementation of the control scheme analyzed in this work. In this chapter are discussed the DNS code, the control scheme developed, and the numerical experiments' setup; a discussion about the total energy balance ends this chapter.

Figure 2.1: *Computational domain.*

2.1 Governing equation and numerical procedures

The reference geometry considered is that of the plane channel and x, y, and z represent the streamwise, spanwise and wall-normal (respect to the wall reference condition) directions, respectively; similarly, u, v and w indicate x-, y- and z-directions velocities as shown in figure 2.1.
In this work the flow is governed by the continuity equation and the unsteady, viscous, incompressible momentum equation which can be written in the following form:

$$\nabla \cdot \mathbf{u} = 0 \tag{2.1}$$

$$\frac{\partial \mathbf{u}}{\partial t} = -(\mathbf{u} \cdot \nabla)\mathbf{u} - \nabla p + \frac{1}{Re}\nabla^2 \mathbf{u} \tag{2.2}$$

where $\mathbf{u}$ represent the velocity vector, p the modified pressure P/ρ, in which ρ is the density, and Re the Reynolds number. Here, all variables are non-dimensionalized by the reference channel semi-height h, and the mean bulk velocity defined as:

$$U_b = \frac{1}{2h}\int_0^{2h} \overline{u}(z)dz \tag{2.3}$$

where $\overline{u}(z)$ represents the mean velocity profile in the channel

$$\overline{u}(z) = \frac{1}{L_x L_y}\int_0^{L_x}\int_0^{L_y} u(x,y,z)dxdy \tag{2.4}$$

in which L_x and L_y are the channel dimensions in the streamwise and spanwise direction respectively. As a consequence, using this convention, the Reynolds number is defined as $Re = U_b h/\nu$ and the non-dimensional time is found to be tU_b/h. Hereafter, quantities are made dimensionless with the channel half-height, h, and the bulk velocity, U_b, defined just above; with $^+$, indicating viscous units, variables are non-dimensionalized using the uncontrolled skin-friction velocity, $u_\tau = \sqrt{\tau_w/\rho}$, if not otherwise specified, and the channel semi-height.

The DNS code solves the incompressible Navier-Stokes equations written in primitive variables on a staggered Cartesian grid. In particular, a finite-difference, second-order method is employed in every direction for the spatial derivatives; the time advancement is carried out by a third-order explicit Runge-Kutta scheme instead. The

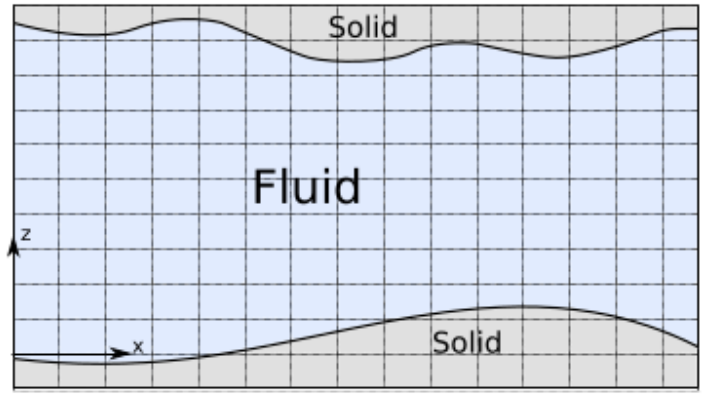

Figure 2.2: *Example of solid boundaries immersed within a fixed uniform grid.*

numerical integration of governing equations is performed using a fractional step approach. In the first step, the momentum equation is updated without taking into account the incompressibility constrain; this is subsequently enforced in the corrector step: an iterative red-black tree algorithm projects the velocity field in a divergence free space and, in the meantime, updates the modified pressure field accordingly.

In the present work, the channel walls are modeled employing an implicit immersed-boundary method. The use of an immersed boundary method gave, in this particular work, an immense advantage: grid generation is trivial and is done once at the beginning of the simulation, neglecting the real wall shape in the mesh generation. For such methods, the computational grid is not body fitted, but solid boundaries are fully immersed within the computational domain as illustrated in figure 2.2. More details about the immersed boundary technique are given by Iaccarino and Verzicco [15] or can be found in [10]. The no-slip condition is applied through a corrective coefficient, $imbc$, in the time advancement. Taking, for example, the x-component of the momentum equation 2.2 that reads

$$\frac{\partial u}{\partial t} = RHS = -\frac{\partial u^2}{\partial x} - \frac{\partial uv}{\partial y} - \frac{\partial uw}{\partial z} - \frac{\partial p}{\partial x} + \frac{1}{Re_b}\left(\frac{\partial^2 u}{\partial x^2} + \frac{\partial^2 u}{\partial y^2} + \frac{\partial^2 u}{\partial z^2}\right) \tag{2.5}$$

discretized, for the sake of simplicity, using a forward Euler scheme it yields to

$$u^{n+1} = u^n + RHS \cdot \Delta t \tag{2.6}$$

Introducing the immersed boundary correction 2.6 becomes

$$u^{n+1} = \frac{u^n + RHS \cdot \Delta t}{1 + imbc \cdot \Delta t} \tag{2.7}$$

in which $imbc$ is the immersed boundary coefficient: far away from the boundary $imbc = 0$ so any correction is applied; differently when a mesh point is inside the solid wall $imbc \to \infty$ (for practical purposes $imbc = 10^{10}$ when a point is inside the wall). As a consequence $u^{n+1} \to 0$ enforcing, in this way, the no-slip condition. Since in the present work the solid boundary could freely move in the z-direction the boundary condition in this specific direction needed to be modified accordingly. In fact, when

a mesh point lies inside the solid boundaries, the z-component of the velocity, w, has to approach the boundary velocity w^w, where the apex w indicates wall values, rather than 0. Hence equation 2.7 needs to be rewritten:

$$w^{n+1} = \frac{w^n + RHS \cdot \Delta t}{1 + imbc \cdot \Delta t} + \frac{imbc \cdot \Delta t}{1 + imbc \cdot \Delta t} w^w \tag{2.8}$$

where, in this case, RHS is the right-hand side of the z-component of the momentum equation, instead. In this way, as a point lies closer and closer to the solid boundary $imbc \to \infty$ and, consequently, the first term on the right-hand side of equation 2.8 tends to vanish while the second term approaches the boundary velocity w^w. On the contrary, far away from the wall $imbc = 0$ so any correction is applied. Given that in the proximity of the solid wall the leading contribution to momentum balance is due to the viscous term, the $imbc$ coefficient results from a correction applied only to the linear term of the momentum equation. Restricting this discussion to a two-dimensional example in which the solid boundary has a non-null vertical velocity w^w, if the grid-node, in which the velocity $w_{(i_x,i_z)}$ is calculated, lies exactly on the wall surface, the discretization of the viscous term in equation 2.2 would read:

$$\begin{aligned} L_{w_{(i_x,i_z)}} =& \frac{1}{Re_b}\left[\frac{w_{(i_x-1,i_z)} + w_{(i_x+1,i_z)}}{\Delta x^2} + \frac{w^w + w_{(i_x,i_z+1)}}{\Delta z^2} + \right. \\ & \left. - \left(\frac{2}{\Delta x^2} + \frac{2}{\Delta z^2}\right) w_{(i_x,i_z)}\right] \end{aligned} \tag{2.9}$$

However, if the grid-node does not lie precisely on the wall surface a more appropriate way of approximating the linear term has to take into account the actual distance, δ, between the node (i_x, i_z) and the boundary:

$$\begin{aligned} L_{w_{(i_x,i_z)}} =& \frac{1}{Re_b}\left[\frac{w_{(i_x-1,i_z)} + w_{(i_x+1,i_z)}}{\Delta x^2} + \frac{w^w}{\delta \Delta z} + \frac{w_{(i_x,i_z+1)}}{\Delta z^2} + \right. \\ & \left. - \left(\frac{2}{\Delta x^2} + \frac{1}{\Delta z^2} + \frac{1}{\delta \Delta z}\right) w_{(i_x,i_z)}\right] \end{aligned} \tag{2.10}$$

Comparing equation 2.9 with equation 2.10 the immersed boundary coefficient results to be, in this particular example, equal to:

$$imbc = \frac{1}{Re_b}\left(\frac{1}{\delta \Delta z} - \frac{1}{\Delta z^2}\right) \tag{2.11}$$

From equation 2.11 it is deductible that as $\delta \to 0$, that is the point approaches the wall surface, the immersed boundary coefficient tends to infinity. In the case of non-stationary walls the immersed boundary coefficients need to be calculated at each time step; the computational time required to complete this task represents about the 30% of the time required to complete the entire time step.

2.2 State-of-the-art of opposition control through wall deformation

Before proceeding in the presentation of the control scheme developed in the present work, is here presented a discussion about the state-of-the-art of the opposition control realized through wall deformation.

Following the successful results of blowing/suction, flow control with active wall motions locally deformed according to opposition control was investigated by Kang and Choi [19] and by Endo, Kasagi, and Suzuki [9].
The former proposed two different types of control:

- in the first the wall deformation velocity was opposite the wall-normal velocity at a given plane: $w_w = -w|_{z^+ \simeq 10}$, in which z^+ is the wall-normal distance in wall units.
- in the second the wall deformation velocity was proportional to the spanwise derivative of the spanwise-velocity gradient at the wall: $\hat{w}_w = C \frac{ik_y}{k} \frac{\partial \hat{v}}{\partial z}|_{wall}$, in which $k = \sqrt{k_x^2 + k_y^2}$ where k_x and k_y are, respectively, the streamwise and spanwise wavenumbers, and the hat denotes the Fourier component.

In their study, they restricted the maximum amplitude of wall deformation to $|z_w^+| \leq 5$ because, without imposing this limit, the root-mean-square wall-deformation magnitude rapidly increased, breaking down the simulations. Starting from a fully-developed turbulent channel flow at $Re_\tau = 140$, they achieved an overall drag reduction of $13 - 17\%$.
Endo, Kasagi, and Suzuki employed a simple feedback algorithm similar to the v-control scheme of Choi, Moin, and Kim [6]: the local velocity of the wall deformation was given to be out-of-phase of the wall-normal velocity in the buffer region

$$w_w^+ = -(w_s^+ - \langle\langle w_s^+ \rangle\rangle) - 0.31 z_w^+ \tag{2.12}$$

in which w_s^+ was the wall-normal velocity at $z^+ \simeq 15$ and z_w^+ indicated the displacement of the wall. The last term of the right hand side was used as a damping term to suppress excessive wall deformation. The double bracket $\langle\langle w_s^+ \rangle\rangle$ denoted an ensemble average of the wall-normal velocity in the xy-plane and was implemented to keep the total volume of the flow domain constant. They obtained a mean drag reduction rate of about 10% at $Re_\tau = 150$. In the last part of their work, they also carried out simulations assuming the control devices to have finite dimensions. The streamwise and spanwise dimensions of the actuator were 172 and $60\nu/u_\tau$, respectively; each actuator was assumed to be deformed only in the z-direction. Shear stress sensors were employed upstream of the actuators' position. Following Lee et al. [25], the wall velocity was determined from the spanwise gradients of the instantaneous wall shear stresses. Adopting this type of control, a maximum drag reduction rate of 17% was obtained.

The control scheme presented in the following section 2.3 is similar to that developed by Endo, Kasagi, and Suzuki. However, it provides several additional possibilities. The sensing plane position is not predetermined, but it can be changed, instead. The coefficient of the control law can be modified as well. Moreover, it is also possible to move the sensing point upstream or downstream of the actuation point. Finally, a new term, depending on the wall acceleration, is introduced.

2.3 Control law

An active feedback control law, based on a linear proportional-integral-differential (PID) controller, is developed. The aim is to achieve a net power saving to sustain the flow in a channel flow. The use of PID controllers allows adequate control of an exceptionally ample number of processes; for this reason, this type of controller is the most commonly used in engineering applications. Besides, simple but effective calibration laws have been elaborated over time. Finally, thanks to their straightforwardness, PID controllers could be manufactured with various technologies such as mechanical, pneumatic, or hydraulic actuators complemented by analog or digital electronics.

In the most general case, in PID controllers, the controlled variable, in this work the wall velocity w^w, is composed of three factors:

- the first is proportional to the error between the input signal and the output variable of the controlled system;
- the second is proportional to the integral of the error and is needed in order to enforce that the latter vanishes asymptotically;
- the third is proportional to the derivative of the error and anticipates its course in the following moments.

The more the proportional constant is increased the faster the system's response is but, at the same time, the more its behavior is oscillatory. The derivative factor could be used to damp those response which have excessive oscillations. The integral term is needed whenever a correction between the desired value and the system output is required for static performances. For a detailed analysis of the PID controllers consult [2] or [4].

Considering channel flow the wall deformation velocity in a certain point (x, y) at time t is given by a term proportional to fluid velocity along z-direction, a term proportional to the wall position with respect to its reference position and, finally, a term proportional to the wall acceleration. The PID control law reads:

$$\begin{aligned} w^w_{(x,y,t)} = &- K_p \cdot w_{(x-\delta x,y,z_c,t)} - K_i \cdot \left(z^w_{(x,y,t)} - z^{w,ref} \right) + \\ &- K_d \cdot \left(w^w_{(x,y,t)} - w^w_{(x,y,t-\Delta t)} \right) / \Delta t \end{aligned} \tag{2.13}$$

in which z_c is the location of the sensing plane and δx makes possible placing the sensing point upstream the actuation point to anticipate the vortices movements. The apex w indicates wall values. Please note that the distance of the sensing plane z_c is taken with respect to the reference wall position and consequently each sensing point does not follow wall movements. In this study no interpolation has been applied to obtain the velocity w at the detection plane z_c; hence, the sensing plane is located at the nearest z grid point around the nominal value. In the same way, when a shift in the x direction is applied, the sensing point is located at the closest streamwise grid point around the nominal value $x - \delta x$. The first term in equation 2.13 is used to realize an opposition control while the second term is necessary to gradually restore the wall to its reference position; if excessive oscillations arise in the simulation the third term could be used to damp the control strength.

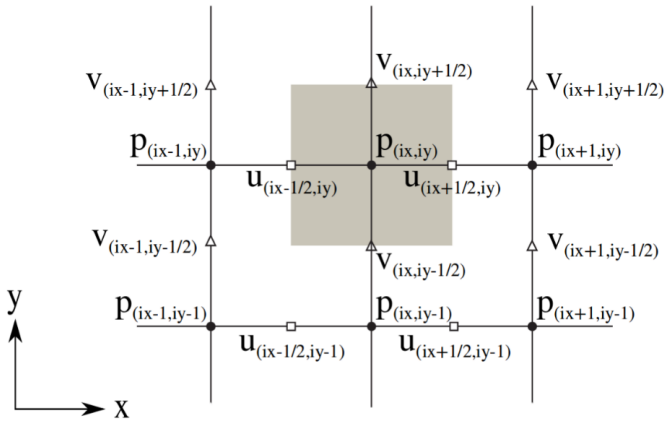

Figure 2.3: *Example of 2D staggered grid adopted in this work.*

Since the fluid velocity w is known only in $n_x \times n_y$ points it is fairly intuitive that even the wall position is known only in some points of the domain. However, given that a staggered mesh has been used as shown in figure 2.3, an interpolation is needed to evaluate the wall position even in the points of coordinates $\big((i_x + 0.5) \cdot \Delta x, i_y \cdot \Delta y\big)$ where the velocity u is calculated and, similarly, in $\big(i_x \cdot \Delta x, (i_y + 0.5) \cdot \Delta y\big)$ where the velocity v is calculated instead; this is necessary to evaluate the immersed boundary correction $imbc$. To do so a linear interpolation has been adopted. For example the wall position, z^w, in the generic point $\big((i_x + 0.5) \cdot \Delta x, i_y \cdot \Delta y\big)$ at time t can be written according to the value on the previous and next node:

$$z^w_{\big((i_x+0.5)\cdot\Delta x, i_y\cdot\Delta y, t\big)} = 0.5 \cdot \left[z^w_{\big(i_x\cdot\Delta x, i_y\cdot\Delta y, t\big)} + z^w_{\big((i_x+1)\cdot\Delta x, i_y\cdot\Delta y, t\big)} \right] \tag{2.14}$$

Moreover, the new wall position at time $t + \Delta t$ is evaluated using a third-order explicit Adams-Bashforth formula:

$$z^w_{(x,y,t+\Delta t)} = z^w_{(x,y,t)} + \frac{\Delta t}{12} \cdot \left(23 w^w_{(x,y,t)} - 16 w^w_{(x,y,t-\Delta t)} + 5 w^w_{(x,y,t-2\Delta t)} \right) \tag{2.15}$$

in which z^w represents the wall position and w^w its velocity.

In order to visualize the control scheme effect in figure 2.4 is reported the z-component of the velocity field, w, in a yz-plane slice of a subset of the entire channel; the cross stream velocity vectors ($v \cdot \hat{y} + w \cdot \hat{z}$) are also highlighted with arrows. The instantaneous wall shape is showed through the thick black line whereas the horizontal thinner line represents the sensing plane location in that specific simulation. In this particular case, the coefficients of the control law are set to:

- $K_p = 1.2$;
- $K_i = 0.6$;
- $K_d = 0$;

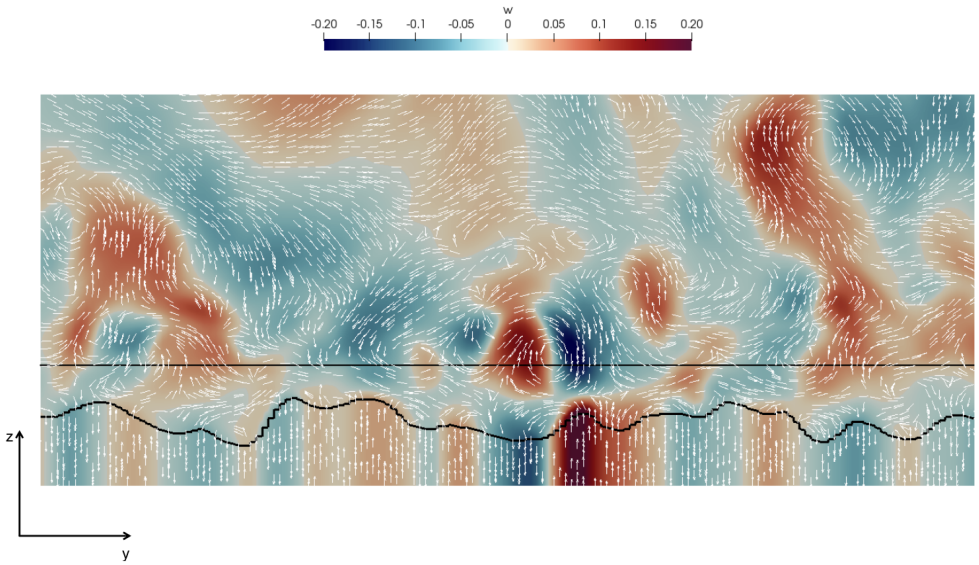

Figure 2.4: *Representation of the control law effect on the wall motion.*

- $z_c = 0.17$;
- $\delta x = 0$.

As it is possible to see nearly in the middle of the figure, where a typical longitudinal vortex is present, the wall movements counteract the sweep fluid motion on one side of the vortex and, equally, the raising fluid motion on the other side of the vortex. On the contrary, where the w velocity of the flow is low, the wall tends to smoothly return to its reference position thanks to the integral term of the control law.

Mentioning the possibility of practical use of the control scheme, the size of the actuators should be comparable to that of the quasi-streamwise vortices and hence should be smaller than 30 viscous units big; furthermore, the timescale of the sensors should be analogous to that of the near-wall velocity fluctuations [20]. Such requirements could be fulfilled by the new developments in micro-electro-mechanical-system devices (MEMS). MEMS actuators are, in fact, adequately small and fast, feature low power consumption, and enable considerable out-of-plane displacement or fluid force [32]; moreover, MEMS are also resistant to adverse environments. Unquestionably, a physical quantity, measurable on the wall surface, and that is well correlated with the velocity fluctuations, needs to be determined. However, several studies dealing with this issue are already available in the literature ([25], [28], [9] to cite some).

2.4 Setup of the numerical experiments

The baseline case is a fully developed turbulent channel flow and simulations are carried out at a bulk Reynolds number $Re_b = U_b h/\nu = 2800$, based on the bulk velocity U_b and the channel semi-height h; this corresponds to a friction Reynolds number $Re_\tau \simeq 180$ based on the unmanipulated wall-shear velocity u_τ and the channel semi-height as well. That particular Reynolds number has been chosen to compare the results with the authoritative and deeply studied channel flow of Kim Moin and Moser (1987) [24].

A computational box of dimensions $L_x = 2\pi$, $L_y = \pi$ in the streamwise and spanwise directions respectively has been used to do a parametric study of the problem first; then a bigger domain of dimensions $L_x = 4\pi$, $L_y = 2\pi$ once again in the streamwise and spanwise directions has been taken into account to validate the previously obtained results. Since an immersed boundary method is used for the computations some extra space was needed in z-direction to accommodate walls movements: in this direction $L_z = 2.6$ for the parametric study and $L_z = 2.4$ for the validation of the results.

In both of these computational domains a uniform grid in the streamwise and spanwise directions is adopted with spacing respectively of $\Delta x^+ = 5.5$ and $\Delta y^+ = 3.2$ based on the unmanipulated wall-shear velocity u_τ.

In the parametric analysis a uniform grid is used even in the z-direction with spacing $\Delta z^+ = 1.5$. For results validation a different mesh with wall refinement is adopted to increase mesh resolution near the wall. More precisely, in the zone where the wall has been expected to move a denser grid with spacing $\Delta z^+ = 0.8$ is implemented, then grid spacing is reduced with a constant growth factor $\varphi = \Delta z^+_{(i_z)}/\Delta z^+_{(i_z-1)} - 1 = 1.9\%$ up to the centerline of the channel where $\Delta z^+ = 3.4$.
All mesh information are summarized in table 2.1.

Table 2.1: *Mesh information.*

Mesh	L_x	L_y	n_x	n_y	n_z	Δx^+	Δy^+	Δz^+_{min}	Δz^+_{max}
Parametric	2π	π	200	160	314	$\simeq 5.5$	$\simeq 3.5$	$\simeq 1.5$	$\simeq 1.5$
Validation	4π	2π	400	350	338	$\simeq 5.5$	$\simeq 3.2$	$\simeq 0.8$	$\simeq 3.4$

Hence computations have been carried out with approximately 10 millions grid points ($200 \times 160 \times 314$, in x, y, z) for the parametric study whereas 47 millions grid points ($400 \times 350 \times 338$, in x, y, z) have been used for the results validation. Using an Intel i7-9700K commercial processor, the core time required for the computation with the latter mesh is about 40 seconds per time step, which includes the three sub-steps of the Runge-Kutta scheme, the evaluation of the immersed boundary coefficient, and the updating of the wall position. In figure 2.5 is reported the time required per time step exploiting an increasing number of cores.

The time step is $\Delta t = 0.01$ in the parametric study and $\Delta t = 0.015$ in the results validation phase; both guarantee that the CFL condition is amply satisfied for the chosen time integration scheme (section 2.1).

Since at least 100 samples are needed to obtain meaningful results sampling is performed every 1 external time unit in the parametric analysis whereas $\simeq 5$ time units in the results validation; this ensures a good statistical accuracy. Three files are saved each sample: one containing the flow field computed variables $(u,\ v,\ w,\ p)$, the other containing the bottom and top wall z-coordinate, respectively.

Periodic boundary conditions are imposed in the homogeneous x- and y-direction whereas the no-slip condition on the solid deformable walls is given as:

$$u = v = 0, \quad w = w^w \ \ \forall\, z \leq z^{b,w} \ \cup \ z \geq z^{t,w} \tag{2.16}$$

in which w^w is the wall velocity given by equation 2.13 and $z^{b,w},\ z^{t,w}$ indicates respectively bottom and top wall position given by 2.15.

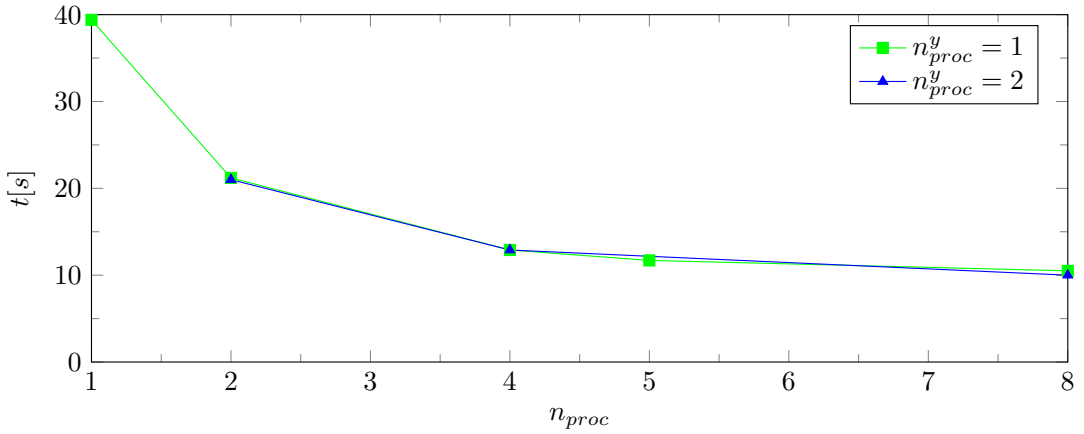

Figure 2.5: *Time required per iteration as a function of the number of cores used; n^y_{proc} is the number of cores used to parallelize the calculation in the spanwise direction.*

In order to reduce input/output operations only points z-coordinate has been stored in two different arrays: z_z and z_d; the former collects the vertical position where the pressure is calculated whereas, the latter, contains the vertical position where both pressure and w velocity are evaluated. Also bottom and top wall vertical position need to be stored in two arrays of dimension $n_x \times n_y$ and, analogously, wall velocity at time t, $t - \Delta t$, $t - 2\Delta t$ are stored in three different arrays. This is necessary to update the new wall position using the Adams-Bashforth scheme adopted in this work for the boundary position updating (see equation 2.15).

2.5 Total dissipation balance

In this work the net power saving rate S is computed from the total dissipation $\mathcal{E}$. In fact, following [12], at the statistically steady state the pumping power plus the power required for wall deformation equal the total dissipation $\mathcal{E}$

$$\mathcal{E} = P_f + P_p + P_i \tag{2.17}$$

where P_f represents the friction power coefficient, P_p the pressure power coefficient and P_i the input power coefficient due to wall deformation. In this study the total dissipation $\mathcal{E}$ and the friction, P_f, and pressure, P_p, contribution were separately calculated from the saved instantaneous flow fields whereas the input power contribution P_i have been deduced from equation 2.17. The total dissipation is evaluated as

$$\mathcal{E} = \frac{2}{Re_b V} \int_V \mathbf{S} : \mathbf{S} dV \tag{2.18}$$

where V is the fluid volume and $\mathbf{S}$ is the strain rate tensor defined as

$$\mathbf{S} = \frac{1}{2}\left(\nabla \mathbf{u} + (\nabla \mathbf{u})^T\right) \tag{2.19}$$

in which the superscript T denotes the transpose. In equation 2.18, the operator : is the double dot tensor product $\mathbf{S} : \mathbf{S} = S_{ij} S_{ij}$. The friction contribution is evaluated as

$$P_f = \frac{1}{Re_b S} \int_S \frac{\partial U_t}{\partial n} dS \tag{2.20}$$

in which U_t denotes the tangential component of the velocity with respect to the wall surface S and n is the normal direction to the wall in the point (x, y). Note that the evaluation of the friction power contribution is not trivial in the case of highly irregular shaped walls. It requires, in fact, the calculation of the tangential component of the velocity to the wall surface for each point of coordinates (x, y). Furthermore, in the present work, the wall is known only for points; as a consequence, the wall slope needs to be approximated using the available data. Moreover, the approximation of the derivative $\partial U_t/\partial n$ is critical for points that are close to the boundary surface. Finally the pressure contribution is calculated as the streamwise component of the pressure force acting on the wall surface properly non-dimensionalized:

$$P_p = \frac{1}{S} \int_S p\mathbf{n} \cdot \mathbf{x} dS \tag{2.21}$$

where p is the modified pressure, $\mathbf{n}$ is the normal unit vector to the wall surface and $\mathbf{x}$ is the streamwise unit vector. In this case, it is necessary to evaluate the normal unit vector in each point of the surface. As aforementioned the net power saving rate is computed directly from the total dissipation:

$$S = \frac{\overline{\mathcal{E}}_{ref} - \overline{\mathcal{E}}}{\overline{\mathcal{E}}_{ref}} \times 100[\%] \tag{2.22}$$

where $\overline{\mathcal{E}}_{ref}$ and $\overline{\mathcal{E}}$ denotes the time averaged total dissipation of the uncontrolled and controlled flow respectively. The time averaged dissipation is simply defined as

$$\overline{\mathcal{E}} = \frac{1}{t_f - t_i} \int_{t_i}^{t_f} \mathcal{E} dt \tag{2.23}$$

where t_i and t_f are respectively the initial and final external time unit. A detailed analysis which examines all contributions of $\mathcal{E}$ will be presented later in chapter 4.

CHAPTER 3

Parametric study

In the first part of this work, a parametric study, changing one at a time the coefficients of the control law (see equation 2.13), has been made. This analysis is mainly aimed to investigate the effect of changing the proportional and integral coefficients, varying the sensing plane location and the streamwise shift, on the net power saving rate; only a few simulations have been done also with the differential term because, in the cases of interest, no oscillations have been observed. The chapter is concluded with a brief analysis of selective control: two simulations have been conducted controlling only sweep motions ($w' < 0$) in the first whereas only ejections ($w' > 0$) in the second.

To perform this study more than 80 simulations have been completed keeping constant the streamwise flow rate and starting from the same initial turbulent flow field. In this analysis, the simulations have been carried out for about 150 time units using approximately 34 core hours each. The main aim of this phase of the work is to examine, for each simulation, the resulting net power saving rate, S, defined in equation 2.22; since the solution reaches the statistically steady state after approximately 20 time units this has been defined here as the mean net power saving rate obtained between 20 and 150 time units to have comparable results. Note that, since the lowest net power required to drive an incompressible, constant mass-flux channel flow is exactly that of the laminar flow, the maximum net power saving rate, at this Reynolds number, is 74%. As stated in section 2.4, to have good statistical accuracy, sampling has been performed every 1 time unit (tU_b/h).

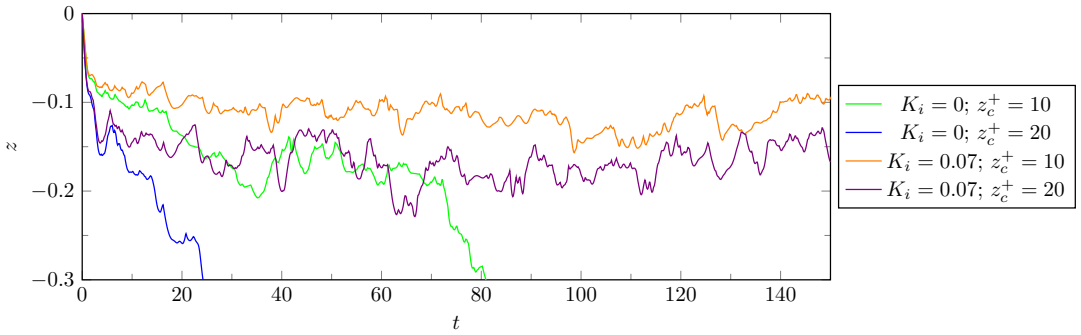

Figure 3.1: *Minimum bottom wall position for different K_i and z_c^+; $K_p = 0.7$.*

3.1 The proportional term

Before proceeding with the analysis of the effects of the proportional term it should be noticed that a merely proportional control could not give the expected results. To demonstrate this assertion four simulations are below outlined setting $K_p = 0.7$, $K_d = 0$, $\delta x = 0$ and varying the sensing plane location which is placed to $z_c^+ = 10$ or $z_c^+ = 20$; the integral term coefficient is set to $K_i = 0$ or $K_i = 0.07$ instead. Even if a reduction of the net required power to drive the flow has been observed, also setting $K_i = 0$, with a pure-proportional control happens that deep grooves, elongated in the streamwise direction, are rapidly dug in correspondence of the streamwise vortices. As a consequence, the wall diverges indefinitely from its reference position as it is possible to deduce in figure 3.1, in which the time trace of the minimum bottom wall position is shown. It is known that away from the wall, approximately for $z^+ > 12$, ejection events dominate with the sweep events [24]; this reason, in conjunction with the fact that the root-mean-square value of w is higher at $z^+ = 20$ than at $z^+ = 10$, could justify why the simulation in which $z_c^+ = 20$ and K_i is null diverges more rapidly than the simulation in which $z_c^+ = 10$. As it is possible to see in figure 3.1, the introduction of a positive coefficient for the integral term, K_i, has the effect of suppressing excessive wall deformation: even a relatively small factor ($K_i = 0.07$) stabilizes the wall position avoiding the creation of deep furrows in the channel wall, which are as worthless as they are detrimental to obtain a net power-saving. Another fundamental factor that has led to the introduction of an integral term, regulated by the coefficient K_i, is the conservation of the total volume of the flow. As for blowing/suction it was mandatory to ensure the conservation of mass flux through the channel, with this strategy is equally important to verify that the mean position of the channel walls remains unchanged respect to their reference position. This last question is verified even for small K_i: the change of the channel semi-height in viscous units is on average of the order of $\Delta h^+ \simeq 10^{-4}$, which could be considered a negligible value.

Proven that a positive K_i is necessary for the stability of the control law, the variation of the net power saving rate with respect to K_p is analyzed fixing $K_d = 0$, $z_c^+ = 20$ and $\delta x = 0$. For each value of the proportional coefficient, K_p, three simulations have been performed with three different values of the integral coefficient: $K_i = 0.2$, $K_i = 0.4$, $K_i = 0.6$. For $K_p = 1.3$ only the cases with $K_i = 0.4$ and $K_i = 0.6$ are reported because for $K_i = 0.2$ the simulation has stopped due to excessive oscillations.

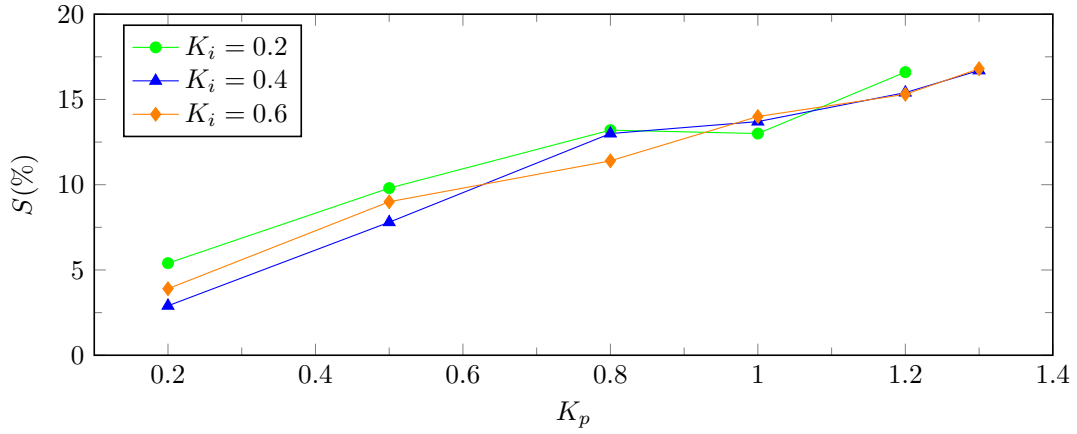

Figure 3.2: *Net power saving rate obtained as a function of K_p for different K_i.*

When $K_p > 1.3$ the cases considered diverges rapidly and are not taken into account here. However, the introduction of a damping factor, $K_d > 0$, allows to further increase the proportional factor K_p beyond 1.3; this possibility is discussed below in section 3.5. Hence, a proportional-integral (PI) control is here adopted having set to 0 the damping term coefficient.

Seventeen simulations have been performed to investigate the effect of varying the proportional coefficient K_p. Generally a higher net power saving rate is accomplished increasing K_p as far as the stability limit, ascertained for $K_d = 0$, $z_c^+ = 20$ and $\delta x = 0$, is reached. With other sets of parameters this limit could be different. Figure 3.2 summarizes the variation of the net power saving rate as a function of K_p for different values of K_i. Furthermore, the growth in the net power saving rate varies almost linearly with the proportional factor.

The effect of diminishing the proportional term is certainly that of reducing the input power required for wall deformation. However, in doing so, the control has a minor effect on the turbulent activity and, as a result, a lower power saving rate is achieved. Table 3.1 summarizes the input power required and the efficiency defined as the ratio between the total power saved and the input power required for wall deformation, $(\mathcal{E}_{ref} - \mathcal{E})/P_i$, for different values of the proportional term fixed $K_i = 0.2$; even if the overbar is omitted the quantities just mentioned are averaged over time. The trend of efficiency shows that increasing the proportional coefficient, the power needed to warp the walls of the channel increases more rapidly than the net power saved. Therefore, the input power plays an increasingly important role in the dissipation balance. Please note that these results can be altered by the limited temporal average; however, the order of magnitude and the trend are nevertheless trustworthy.

When K_p is raised above 1 and K_i is relatively small (that is < 0.4) oscillations in the solution could arise if $K_d = 0$ and simulations could even blow up. This oscillatory behavior is similar to that encountered with zero-net mass flow rate blowing and suction when the proportional constant is, similarly, increased above 1 [22]. For these cases, the introduction of a damping factor ($K_d \simeq 10^{-3}$) eliminates the oscillations. Nonetheless, a detailed analysis of the damping term has not been conducted because, in this phase, the introduction of another free parameter in the control scheme would have excessively

Table 3.1: *Input power required for wall deformation and control efficiency as a function of K_p fixed $K_i = 0.2$.*

K_p	P_i	$(\mathcal{E}_{ref} - \mathcal{E})/P_i$
0.2	$8.6 \cdot 10^{-5}$	6.1
0.5	$5.1 \cdot 10^{-4}$	1.4
0.8	$7.7 \cdot 10^{-4}$	1.4
1	$1.1 \cdot 10^{-3}$	0.9
1.2	$1.3 \cdot 10^{-3}$	0.8

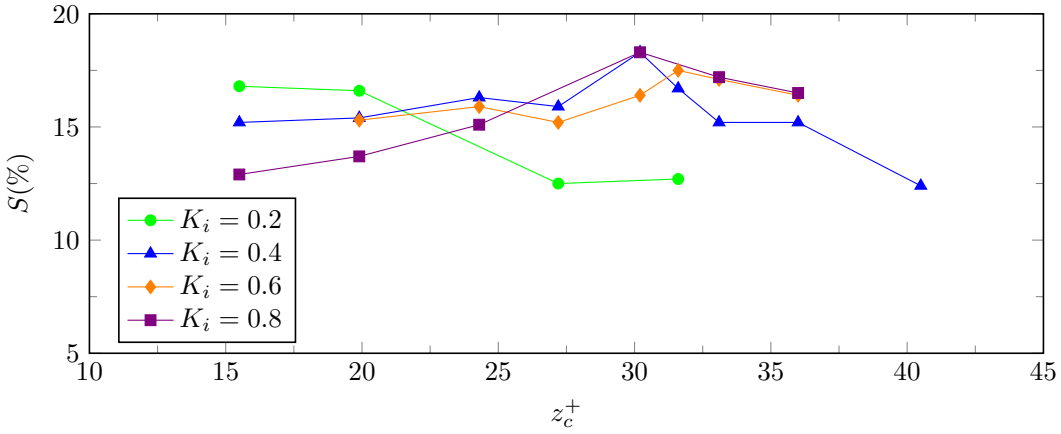

Figure 3.3: *Net power saving rate obtained as a function of z_c^+ for different K_i.*

complicated the study.

Since it is found that a greater net power saving rate is achieved increasing the proportional coefficient, at least up to the stability limit of the control law, in figure 3.3 is reassumed the net power saving rate trend as a function of the sensing plane location, z_c^+, for different integral coefficients, K_i, fixed $K_p = 1.2$, $K_d = 0$ and $\delta x = 0$. As it is possible to see a better net power saving rate is obtained when the detection plane is placed around $z_c^+ = 30$. However, the net power saving rate varies only by about 5% even considering very different sensing plane locations and integral coefficient values. For $z_c^+ = 15$, the net power saving rate achieved is higher than that shown by Endo et al. in his work [9], in which an analogous control scheme is used.

3.2 The integral term

Subsequently many K_i values have been tested setting $K_d = 0$, $z_c^+ = 20$ and $\delta x = 0$. A net power saving has been achieved for a relatively wide range of different integral coefficients K_i as figure 3.4 demonstrates. In the same figure, the trend for four different values of the proportional coefficient is reported. The main role of the integral term is to limit wall excursion from its reference positions as it is possible to see in figure 3.5, in which the minimum position of the bottom wall, fixed $K_p = 1.2$, is shown: the more the integral coefficient is increased the less the maximum displacement of the wall from its reference position is.

The same conclusion is reached looking at the root-mean-square (rms) value of the

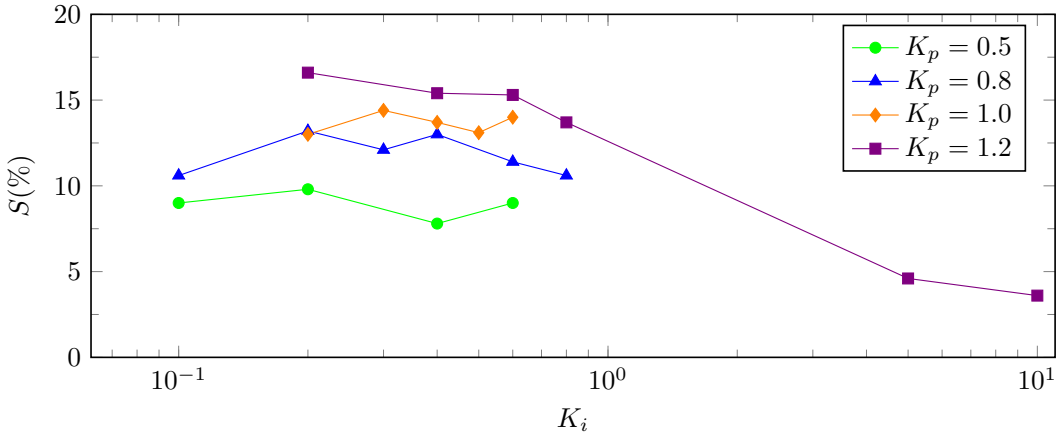

Figure 3.4: *Net power saving rate obtained as a function of K_i for different K_p.*

wall displacement for $K_p = 1.2$. If $K_i = 10$ the rms value of the wall displacement is fairly small, $z^{+,w}_{rms} = 0.7$. It is known that wall roughness within $z^+ = 5$ could be categorized as hydraulically smooth and considered to have a minor effect on the turbulent flow field. Conversely, when $K_i = 0.2$, the rms value is one order of magnitude bigger: $z^{+,w}_{rms} = 7.1$. As a consequence, the flow behavior is certainly influenced by the instantaneous wall shape. Once again setting $K_p = 1.2$ but looking at the root-mean-square value of the wall velocity, instead, when $K_i = 10$, it is found to be $w^{+,w}_{rms} = 0.23$ whereas, for $K_i = 0.2$, it was $w^{+,w}_{rms} = 0.41$; this latter is close to the rms value of velocity fluctuation at $z^+ = 20$ where the sensing plane is positioned. From these considerations it is probable that, for $K_i = 10$, the integral term dominates over the proportional term causing the drop in the effectiveness of the control noticeable in figure 3.4. Nevertheless, leaving apart extreme cases, the effect, if any, of the integral term on the net power saving rate is still unclear.

A possible problem that could occur if K_i is small, let's say ≤ 0.2, is that the control point could be incorporated by the solid boundary, particularly if the control plane is placed nearby the wall reference position. Since the code does not intervene with any restrictions if the wall approaches the sensing plane location, it is mandatory to choose appropriate factors for the control law and to check both the maximum position of the bottom wall and the minimum position of the top wall, to prevent that fact to happen. From all these considerations, it is possible to state that the range between $K_i \simeq 0.3$ and $\simeq 0.6$ gives the best compromise between the wall excursion and the net power saving rate achieved. However, the most appropriate value for the integral term coefficient depend on the proportional coefficient value and the sensing plane location. Few modifications to the current control scheme, limiting the maximum wall deformation while preserving the integral coefficient relatively low, should be implemented in a continuation of the present work to establish whether a higher net power saving rate could be achieved.

3.3 The detection plane location

As for the proportional, K_p, and integral, K_i, coefficients, the effect of the detection plane location on net power saving rate is now examined fixing $K_i = 0.4$, $K_d = 0$ and

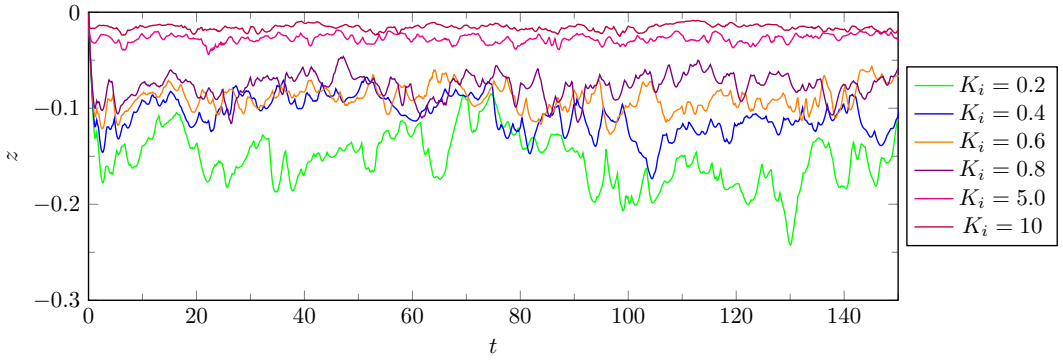

Figure 3.5: *Minimum bottom wall position for different K_i values; $K_p = 1.2$.*

$\delta x = 0$.

In the classical opposition control, the optimal plane location was $z^+_{c,opt} = 15$, whereas a substantial drag increase was found placing the detection plane further than 20 viscous units from the wall surface. Furthermore, a sudden drop in the effectiveness of the control was determined whenever the sensing plane was moved just a little away from $z^+_c = 20$; at $z^+_c = 23$, opposition control became unstable, and drag increase was observed, instead. It should be mentioned here that the location of the sensing plane affects both the amplitude and the phase of the control. Chung and Talha demonstrated that, for $z^+_c > z^+_{c,opt}$, a better drag reduction was achieved reducing the proportional coefficient of the control law. Moreover, it was proven that two velocity signals, even with a good correlation, could result in a completely different control performance; this suggests that the phase information of the detection plane alone cannot explain the sudden change in drag reduction observed [7].

Differently, with the control strategy developed in this work, a net power saving has been achieved for a more extended range of the sensing plane location. However, considering that each control point cannot be incorporated by the solid boundary, the lower position of the sensing plane location is bounded by the wall excursion from its reference position. Although it is possible to increase the value of the integral term coefficient, K_i, to limit wall excursion enabling, in this way, the positioning of the sensing plane closer to the wall, this appears not to be convenient. To give a reference, setting $K_p = 1.2$, $K_i = 0.8$, $K_d = 0$ and $\delta x = 0$ and placing the sensing plane at $z^+_c \simeq 15$, the net power saving rate is 12.5%; this value is below to that obtained locating the detection plane further away from the wall reference position.

As it is possible to see in figure 3.6, the net power saving rate is substantially constant between $z^+_c \simeq 24$ and $\simeq 32$ showing only a couple of percentage points of difference in simulations with the same proportional coefficient. It is meant as a reminder here that, in this analysis, $K_i = 0.4$, $K_d = 0$ and $\delta x = 0$. The small difference in the net power saving rate obtained for various sensing plane locations using the same proportional coefficient could be given by the fact that the root-mean-square value of the w-component of the velocity tends to saturate for $z^+ > 25$. This seems to be confirmed by the rms value of the wall deformation velocity which is almost constant when $24 \leq z^+_c \leq 30$. Furthermore, it is known from the quadrant analysis that even the contribution of the various events (that depends on the sign of the velocity fluctuations) to the total production of turbulence has minimal variations for $z^+ > 25$; this means that

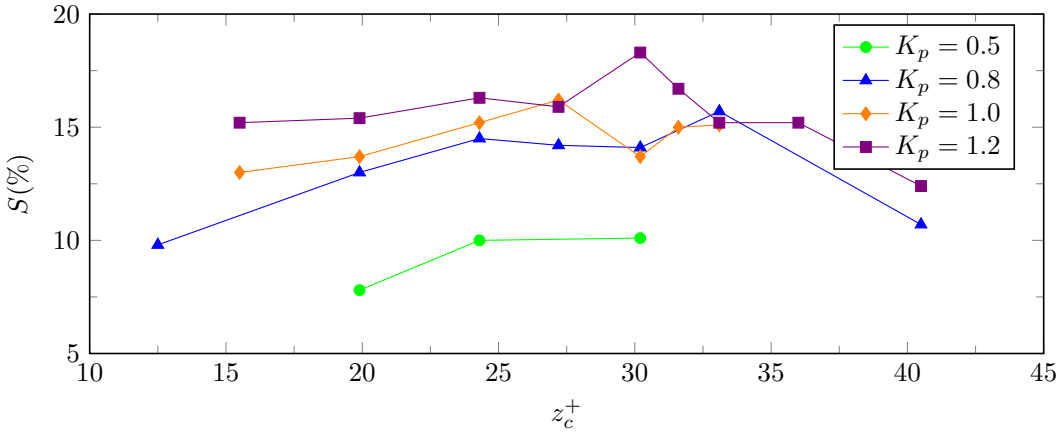

Figure 3.6: *Net power saving rate obtained as a function of z_c^+ for different K_p.*

the share of each contribution to total production remains unchanged.

If the distance between the detection plane and the mean wall position is further increased, there is a decrease in the net power saving rate; this is similar to what happens in the classical opposition control. However, the effectiveness of the opposition control, accomplished through wall deformation, does not deteriorate so much to give drag increase neither when z_c^+ is set to 40. Furthermore, this reduction could be mostly attributable to an increase in the input power required for wall deformation rather than an increase in the shear-friction contribution. Keep in mind that the pressure contribution, and hence the form drag due to the wall shape, is found to be negligible in all cases. Some noteworthy data for $K_p = 1.2$ are shown in table 3.2; these results have been temporally averaged over only 40 time units from 21 saved flow fields and, consequently, could be affected by the small temporal average.

Table 3.2: *Non-dimensional rms value of wall deformation and velocity, friction and input power contribution fixed $K_p = 1.2$ for different z_c^+.*

z_c^+	$z_{rms}^{+,w}$	$w_{rms}^{+,w}$	P_f	P_i
20	5.6	0.38	$6.1 \cdot 10^{-3}$	$7.6 \cdot 10^{-4}$
24	6.0	0.47	$5.7 \cdot 10^{-3}$	$9.4 \cdot 10^{-4}$
27	7.2	0.56	$5.8 \cdot 10^{-3}$	$1.1 \cdot 10^{-3}$
30	7.1	0.59	$5.7 \cdot 10^{-3}$	$1.1 \cdot 10^{-3}$
33	7.4	0.65	$5.7 \cdot 10^{-3}$	$1.3 \cdot 10^{-3}$
36	7.6	0.69	$5.6 \cdot 10^{-3}$	$1.3 \cdot 10^{-3}$
40	7.8	0.79	$5.8 \cdot 10^{-3}$	$1.6 \cdot 10^{-3}$

These results show substantial differences in the flow behavior between blowing/-suction and this specific opposition control strategy. In particular, the opposition control realized through wall deformation has proven to be much less sensitive in sensing plane positioning with respect to suction and blowing. On the other hand, however, the input power needed seems to be quite higher, resulting in a lower net power saving.

The rather large difference obtained for $z_c^+ = 30$ and $K_p = 1$ respect to $K_p = 1.2$, noticeable in figure 3.6, should only be charged to the small temporal average available

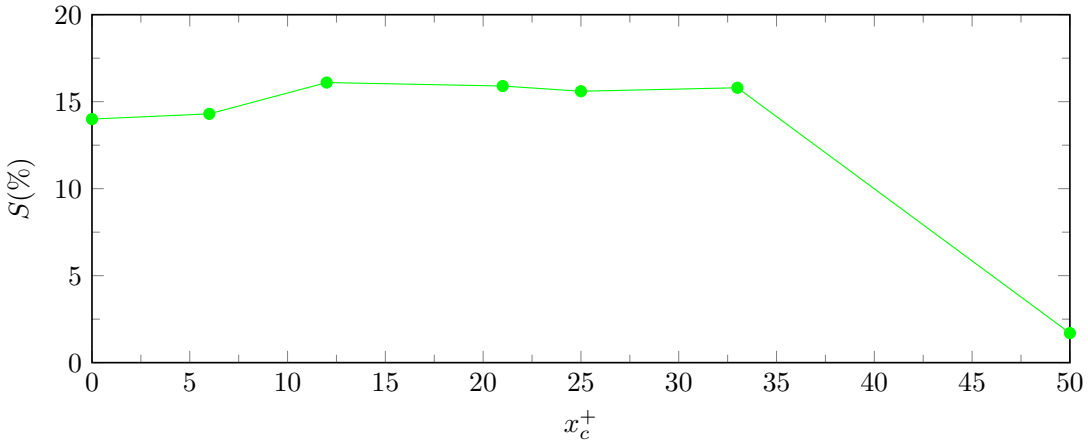

Figure 3.7: *Net power saving rate obtained as a function of* δx^+.

in these simulations.

3.4 The streamwise shift

A possible cause of the relatively small net power saving rate so far reached in the analysis is that the sensing point has been placed precisely above the actuation point. Furthermore, it is known that, in channel flow, the streamwise direction is a preferred direction where velocity perturbations propagate [23]. Therefore, in the attempt to obtain a further reduction in velocity fluctuations, and hence in turbulence, the sensing point is placed upstream of the actuation point. The parameter that regulates the distance between the sensing and the actuation points is δx to which reference is made, in this work, with the name of the streamwise shift. A simulation placing the sensor downstream the actuation point has been also made but, since it has provided drag increase, as expected, it will be not discussed in this section. In this latter analysis the other parameters of the control law were set to: $K_p = 1$, $K_i = 0.6$, $K_d = 0$ and $z_c^+ = 20$. In the opposition control realized exploiting suction and blowing on the wall, it was proven that a slightly higher drag reduction rate could be achieved placing the detection point at $\delta x^+ = 26.2$ upstream the actuation point and the sensing plane at $z_c^+ = 20$ away from the wall [27]. On the contrary, when δx was further increased, an abrupt drop in drag reduction or even drag increase has been demonstrated.

Similarly, with this flow control strategy, a small positive δx gives a lightly better net power saving rate, as shown in figure 3.7. The optimal value seems to be slightly lower than that observed for the classical opposition control, realized applying suction and blowing on the wall. The most effective δx, with this specific set of parameters, is $\delta x = 12$. However, as for the detection plane location, the variation of the net power saving rate is relatively small for an extensive range of streamwise shift values. In general, it is possible to state that the optimal streamwise shift, δx, for the control using the upstream sensor, is determined to be between $\delta x^+ = 12$ and 35. On the contrary, placing the sensor too far from the actuation point has the effect of deteriorating the performances of the control. When $\delta x^+ = 50$, the control scheme is much less effective, showing a sudden drop in the net power saving rate achieved; probably, this reduction could occur

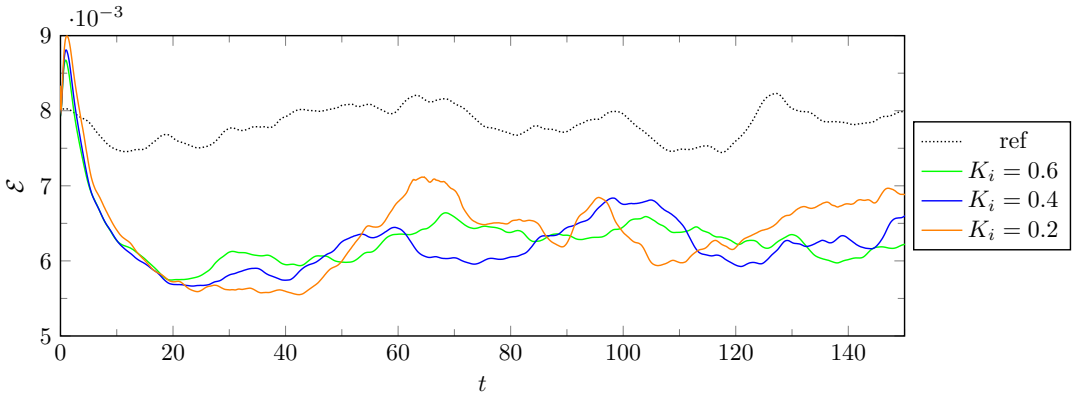

Figure 3.8: *Time trace of the total dissipation as a function of K_i.*

for even smaller δx.

3.5 The differential term

As stated in section 3.1, the differential term could be used for both increasing the proportional coefficient above 1.3 and damping the control strength in those simulations that exhibit oscillatory behavior. In this section three simulations setting $K_p = 1.4$, $K_d = 0.002$, $z_c^+ = 30$ and $\delta x^+ \simeq 18$ are presented; in these simulations the integral coefficient, K_i is respectively set to:

- 0.6 in the first;
- 0.4 in the second;
- 0.2 in the last.

The time trace of the total dissipation is shown in figure 3.8; as it is possible to see no oscillations are present. The net power saving rate obtained in each simulation is summarized in table 3.3 instead.

Table 3.3: *Net power saving rate S obtained through the PID control.*

K_i	0.6	0.4	0.2
$S[\%]$	20.9	21.3	18.9

This brief analysis highlights the need to deepen what could be achieved in terms of the net power saving rate through the PID control in a continuation of the present work. This could be performed with the help of a genetic algorithm to increase the efficiency in the solution of the optimization problem.

3.6 Selective control

It is well established that skin-friction is highly intermittent in turbulent flows. In particular, high skin-friction zones are proven to correspond to downward, high speed,

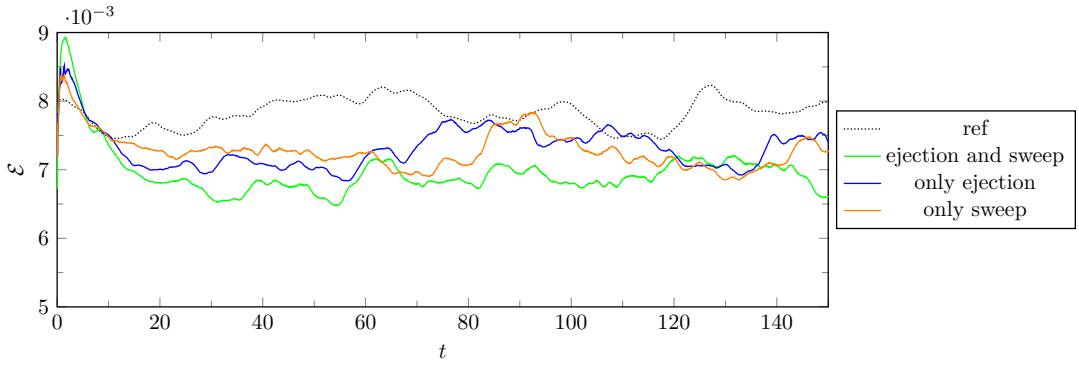

Figure 3.9: *Time history of the total dissipation rate obtained with selective control.*

fluid movement: the sweep events. On the contrary, ejection events are responsible for the production of new turbulence but are associated with low skin-friction zones. In the classical opposition control approach, both sweep and ejection are counteracted lowering, at the same time, the intensity of high and low skin-friction zones. It was demonstrated that blowing only opposition control could be much more effective when compared to standard opposition control [34]. Consequently, two simulations controlling, in the first, only sweep events that are characterized by $w' < 0$, whereas only ejections, $w' > 0$, in the second have been conducted in the attempt of increasing the net power saving rate; these simulations are compared to a simulation performed controlling both sweep events and ejections. While the control of both events characterized by $w' < 0$ and $w' > 0$ kept negligible the change of the channel semi-height, selective control implies that the mean wall position has to be accordingly modified at each time step to guarantee the conservation of total volume. Consequently, some modifications were introduced to the code to apply selective control and to satisfy volume conservation. In these simulations, the parameters of the control law were set to:

- $K_p = 1$;
- $K_i = 0.2$;
- $K_d = 0$;
- $z_c^+ = 20$;
- $\delta x = 0$.

The results show that controlling both ejection and sweep is, with this specific set of parameters, more effective. The net power saving rate by imposing these parameters on the control scheme and counteracting both sweep and ejection is determined to be $S = 13.2\%$. The control of sweep motions or, vice-versa, ejections alone provides a very similar result: the mean net power saving rate achieved is $S \simeq 8.5\%$. This is a surprising result since the control of sweep motions alone is supposed to be more efficient if compared to controlling only ejections. That could be caused by two factors. The first is that at $z_c^+ = 20$, where the detection plane is placed, ejections are more frequent than sweep. The other is that this control strategy could be much less effective in counteracting sweep motions respect to the classical opposition control. In figure 3.9

is reported the time trace of the total dissipation: as it is possible to see the green curve, corresponding to the simulation in which both ejections and sweep are counteracted, is generally below both the blue and the orange curve, which, differently, are related to the selective control.

CHAPTER 4

Analysis of the best-performing cases

In the analysis previously discussed in chapter 3, the domain dimensions are 2π and π in the streamwise and spanwise direction, respectively; below these values, the results may not be reliable. Moreover, even in the z-direction, a uniform mesh is used, causing a lack in the resolution in the near-wall region respect to a refined mesh, using the same number of points. For the above reasons, a couple of numerical simulations, based on the beforehand examined results in chapter 3, have been replicated with a larger domain to uphold the results; furthermore, a denser mesh has been employed in the region where the wall was supposed to move to achieve a better resolution. The resolution in the streamwise and spanwise directions is the same as the parametric analysis. Additionally, in the parametric analysis, simulations were carried out only for 150 time units; that is sufficient to verify the efficiency of the control but is not enough to compute accurate statistics. In the following analysis instead, the computations have been carried out for about 650 time units; the total time required for each simulation was almost 120 CPU hours. Sampling is performed every 5.25 external time units to ensure good statistical accuracy. A detailed explanation of the numerical experiment's setup is given in section 2.4.

The differences between the net power saving rate resulted from the parametric study and that calculated in the following analysis are at most of the order of 1%, which indicates satisfactory reliability of the results previously shown in chapter 3. Besides, a more in-depth analysis of flow statistics has been carried out. All results have been compared with a turbulent plane channel flow that serves as a reference.

4.1 Reference plane channel

To set a reference, with which the flow statistics calculated in all other simulations could be compared, a plane channel flow has been taken into account first. Even this simulation has been carried out for about 650, and sampling has been performed every 5.25 external time units. The calculated mean flow properties, reported in table 4.1, are in good agreement with the data reported by Kim, Moin, and Moser [24] (KMM). In table 4.1 the subscript c indicates channel center-line values and δ^* and θ are the displacement and momentum thickness, respectively. The skin-friction coefficients C_f and C_{f_0} are made dimensionless using respectively the mean bulk velocity and the mean centerline velocity.

Table 4.1: *Mean flow properties.*

	ref	KMM
$Re_b = U_b h/\nu$	2800	≈ 2800
$Re_\tau = u_\tau h/\nu$	176.8	≈ 180
$Re_c = U_c h/\nu$	3271	≈ 3300
u_τ	0.063	0.064
$C_f = \tau_w/(0.5\rho U_b^2)$	$7.98 \cdot 10^{-3}$	$8.18 \cdot 10^{-3}$
$C_{f_0} = \tau_w/(0.5\rho U_c^2)$	$5.85 \cdot 10^{-3}$	$6.04 \cdot 10^{-3}$
U_b/u_τ	15.83	15.63
U_c/u_τ	18.5	18.2
U_c/U_b	1.17	1.16
δ^*/h	0.144	0.141
θ/h	0.088	0.087
$H = \delta^*/\theta$	1.63	1.62

In figure 4.1 is shown the mean velocity profile in viscous units. Within the sublayer, $y^+ < 5$, the computational results follow the linear law of the wall (dotted line). In the logarithmic region, a little discrepancy has been found between the calculated u^+ and both the logarithmic law (dash-dotted line) and the results of Kim, Moin, and Moser (KMM, dash-dot-dotted line). This reflects the slightly lower value found for Re_τ noticeable in table 4.1. A possible cause could be the slight lack in temporal average as well in spatial resolution in the near-wall region where $\Delta z^+ = 0.8$; however, because it is required an extended area in which the mesh is refined, it has been practically impossible to increase the near-wall mesh resolution. Another cause could be addressed to the fact that in [24] a spectral method was used. Root-mean-square velocity fluctuation u_{rms}, v_{rms} and w_{rms}, normalized by the uncontrolled skin-friction velocity u_τ, are reported in figure 4.2. Comparison of these results with those of Kim, Moin, and Moser (KMM) shows excellent agreement for all three components. Additionally, the Reynolds shear stress, shown in figure 4.3, normalized with the wall-shear velocity, excellently agrees with the data presented in [24].

4.2 Active control

Subsequently, two simulations with active wall deformation have been performed. In the first one, the sensing point has been placed precisely above the actuation point, $\delta x^+ = 0$; vice-versa, in the second, the sensing point has been shifted upstream the

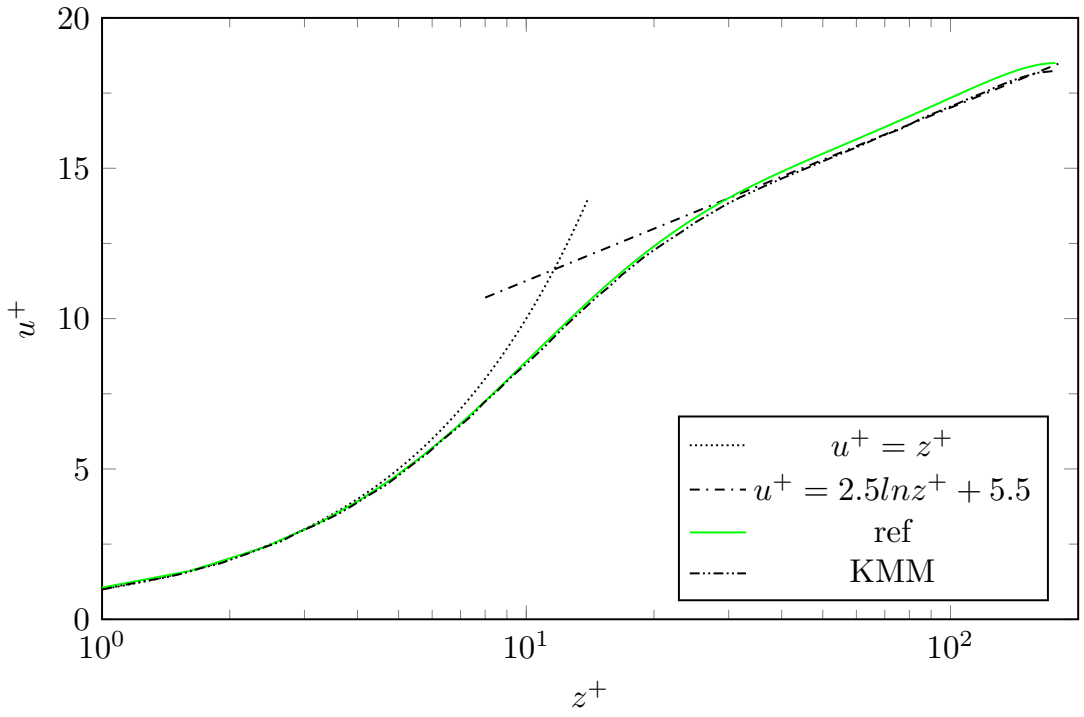

Figure 4.1: *Mean velocity profile.*

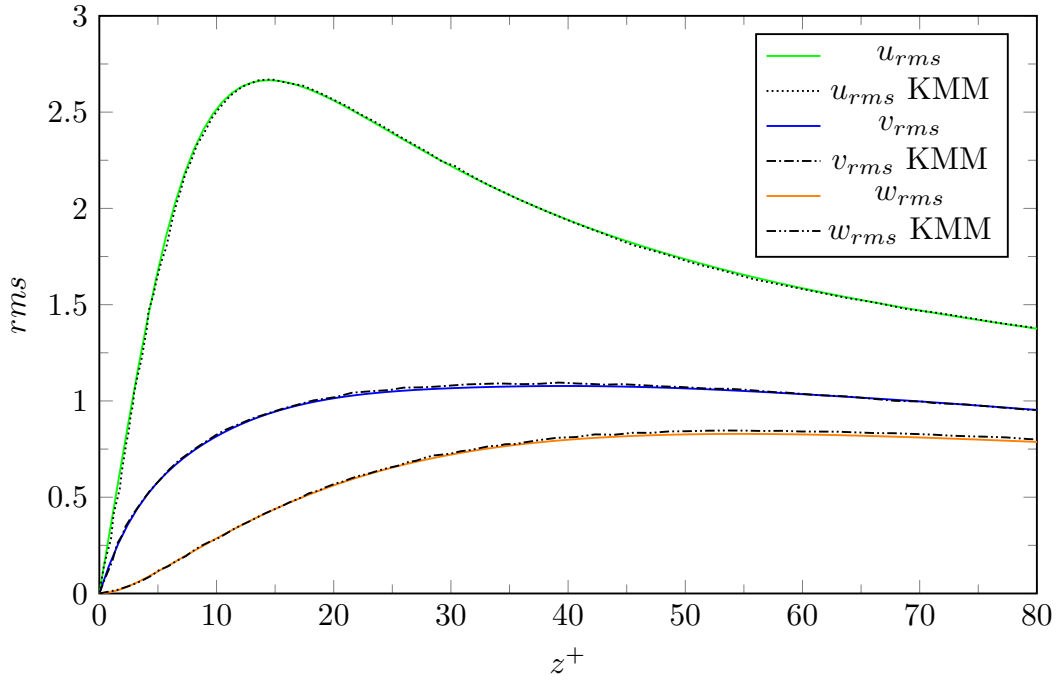

Figure 4.2: *Root-mean-square velocity fluctuations normalized by the wall-shear velocity.*

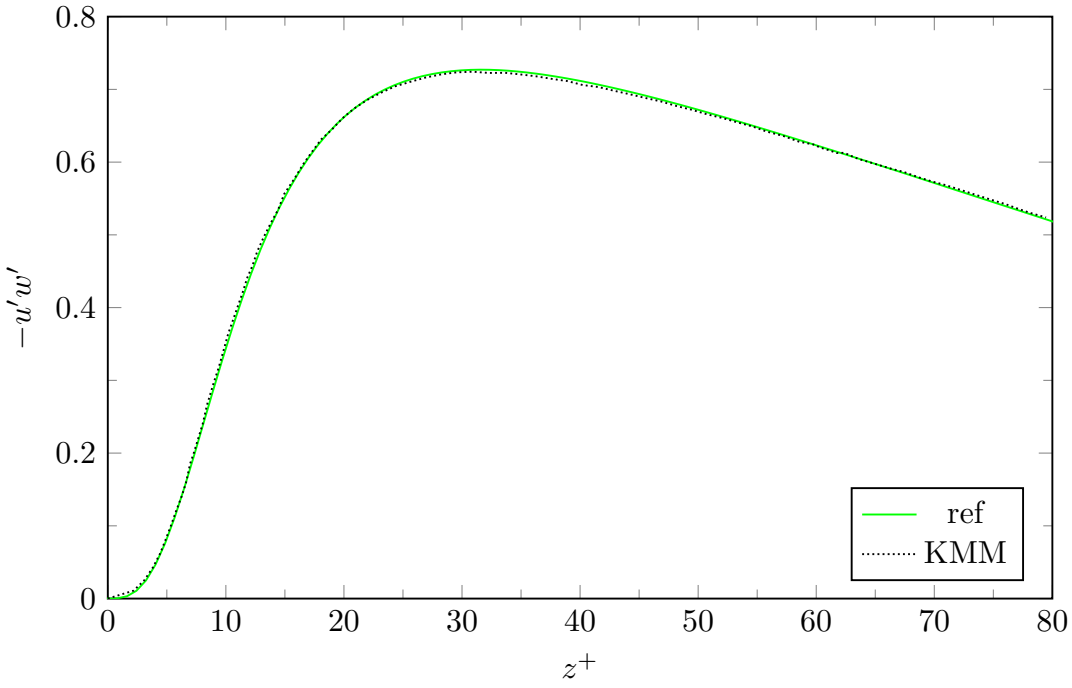

Figure 4.3: *Reynolds shear stress normalized by the wall-shear velocity.*

actuation point: $\delta x^+ = 13$. Taking into account the considerations given in chapter 3, the other parameters of the control law are set to:

- $K_p = 1.2$
- $K_i = 0.6$
- $K_d = 0$
- $z_c^+ = 30$

Note that, as mentioned in chapter 2, the sensing point is not precisely located at $z_c^+ = 30$ away from the wall reference position, as well at $\delta x^+ = 13$ upstream the actuation point, but, at the nearest grid point around these nominal values. Simulation parameters are summarized in table 4.2; here two different friction velocities are used: the uncontrolled wall-shear velocity u_τ, and the mean actual wall-shear velocity u_τ^*. The latter has been derived from the actual wall shear and it is defined as $u_\tau^* = \sqrt{\nu \partial U_t / \partial n}$, in which U_t represents the tangential component of the velocity respect to the wall surface in the point (x, y) whereas n denotes the wall-normal direction; that value has been subsequently averaged both in space and time.

The instantaneous wall deformation and the streamwise velocity (u) at $z^+ = 30$, related to the simulation in which the upstream sensor is used, are shown in figure 4.4: regions in which the wall moves below its reference position are, in general, associated with low speed fluid regions; vice-versa, where the wall raised above its reference position, the streamwise fluid velocity is higher than its mean at that specific xy-plane. The primary scope is, indeed, to counteract high-speed fluid inrush and ejection of low-speed fluid away from the wall. The near-wall coherent structures and the instantaneous

Table 4.2: *Numerical parameters used in the simulations; plus values are made dimensionless using the unmanipulated wall-shear velocity u_τ, whereas starred values are nondimensionalized with the actual wall-shear velocity u_τ^*.*

Case	K_p	K_i	K_d	z_c^+ (based on u_τ)	z_c^* (based on u_τ^*)	δx^+ (based on u_τ)	δx^* (based on u_τ^*)
no-shift	1.2	0.6	0	30.2	26.0	0	0
shift	1.2	0.6	0	30.2	25.7	11.1	9.4

wall deformation are shown in figure 4.5. Only the lower half of the channel is shown to have a better view. The near-wall structures are highlighted using the Q criterion. This is one of the most popular vortex identification methods, and it was firstly proposed by Hunt in 1988 [14]. Q can be expressed as

$$Q = \frac{1}{2}\left(\|\mathbf{R}\|_F^2 - \|\mathbf{S}\|_F^2 \right) \tag{4.1}$$

in which $\mathbf{S}$, $\mathbf{R}$ are the symmetric, $1/2(\nabla\mathbf{u} + (\nabla\mathbf{u})^T)$, and anti-symmetric, $1/2(\nabla\mathbf{u} - (\nabla\mathbf{u})^T)$, parts of the velocity gradient tensor, respectively; the subscript F indicates the Frobenius norm [43]. The appropriate threshold is required to identify vortex structures properly; however, there is no single proper threshold but different thresholds would present different vortex structures. The density of structures isolated by the Q criterion decreases as the threshold increase: in figure 4.5, the isosurfaces for $Q = 1$ are shown. In figure 4.5a, the coherent structures, at $t = 0$, are shown; here, the control is not active yet, and the wall is flat in its reference position. It is evident from 4.5b, instead, that the wall deformation is elongated in the streamwise direction in correspondence of the near-wall coherent structures. Both Hendo [9] and Kang [19] described a similar wall shape in their studies. Turbulent structures appear to be clustered along the grooves dug by the upward motion of the low-speed streaks. It is highly probable that the wall shape and the near-wall turbulent structures influence each other, reducing, in this way, the effectiveness of the control scheme.

4.2.1 Total dissipation and its contributions

The net power saving rate and the total dissipation are summarized in table 4.3; in the same table are reported also the calculated friction (P_f), pressure (P_p) and input power (P_i) contributions. A detailed explanation of how these quantities are evaluated is given in section 2.5. Here the net power saving rate has been defined as the mean net power saving rate obtained between 20 and 650 time units. The time history of the total dissipation, $\mathcal{E}$, and the skin-friction contribution, P_f, are shown in figure 4.6, instead. Note that, since the pressure contribution is resulted small compared to $\mathcal{E}$ ($\approx 1.5\%$), the difference between the two curves corresponds approximately to the time history of the properly non-dimensionalized input power required for wall deformation.

By referring to table 4.3, in the unmanipulated channel, the total dissipation balances exactly the power loss caused by the action of skin-friction, except for a small calculation error ($< 0.04\%$); in fact, there is nor pressure contribution nor input power required for wall deformation as it is stationary. It is meant as a reminder here that the total dissipation ($\mathcal{E}$), the friction contribution (P_f), and the pressure contribution

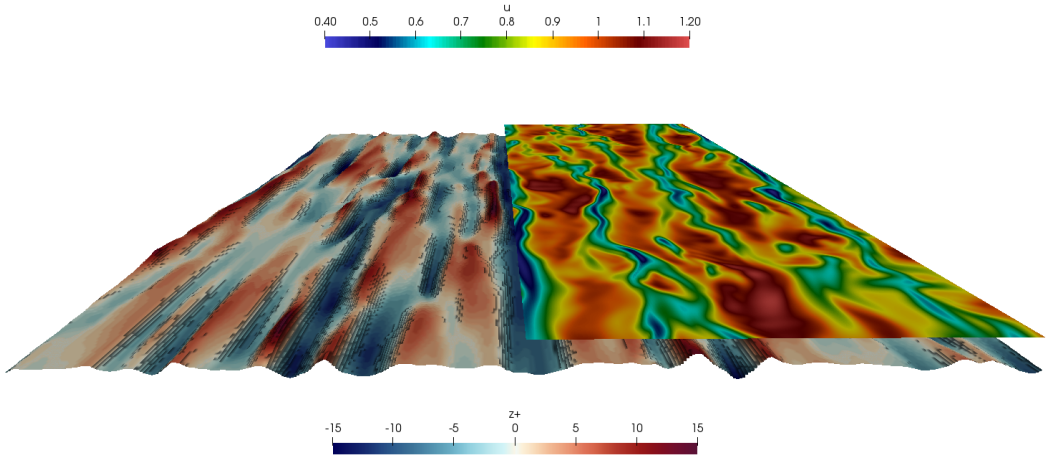

Figure 4.4: *Instantaneous wall deformation and streamwise velocity at $z^+ = 30$, $tU_b/h = 504$; flow moves outward.*

Table 4.3: *Net power saving ratio and contribution to the total dissipation $\mathcal{E}$.*

Case	$S[\%]$	$\mathcal{E}$	P_f	P_p	P_i
plane		0.007980	0.007977	0	0
no-shift	16.7	0.006647	0.005855	−0.000103	0.000895
shift	19.3	0.006441	0.005745	−0.000113	0.000809

(P_p) have been separately calculated from the saved flow fields; conversely, the input power contribution has been evaluated from equation 2.17. In particular, the total dissipation is given by an integral extended to the whole volume of the fluid. The friction power contribution, instead, is provided by an integral over the top and bottom wall surface. The pressure contribution, which is calculated as the x-component of the pressure force acting on the wall surface (see equation 2.21), is found to be weakly negative. That implies that the flow is slightly pumped by the wall motion. However, its value could be considered negligible if compared to the total dissipation ($\mathcal{E}/|P_p| \approx 60$). An analogous result was reported even by Endo, Kasagi, and Suzuki [9]. On the contrary, the input power required for wall deformation is found to be of the order of 10% of the total dissipation. Therefore, the principal loss in the effectiveness of the control respect to zero-net mass flow rate blowing and suction is imputable to a higher input power required. It is noteworthy that this strategy would give roughly the same drag reduction rate achieved with the classical opposition control approach ($25 - 30\%$), observing only the value of the friction contribution. This result is of extreme importance because it highlights that the opposition control, realized through wall deformation, has nearly the same effect on the drag reduction than the classical opposition control. However, if for blowing/suction the input power required was negligible (in the optimal case $P_f/P_i \approx 30$) [7], with the control strategy developed in this work this is unquestionably not the case. The net power saving rate achieved reveals a little improvement with

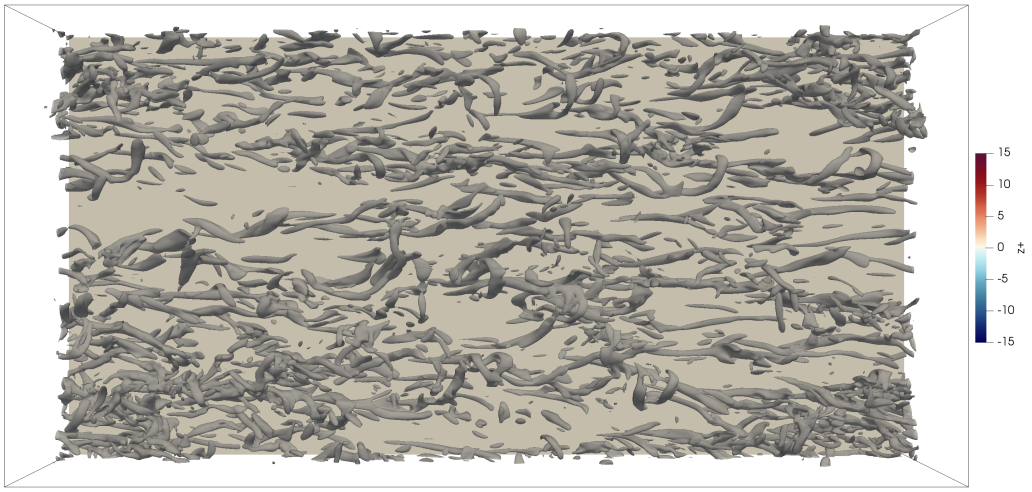

(a) $tU_b/h = 0$.

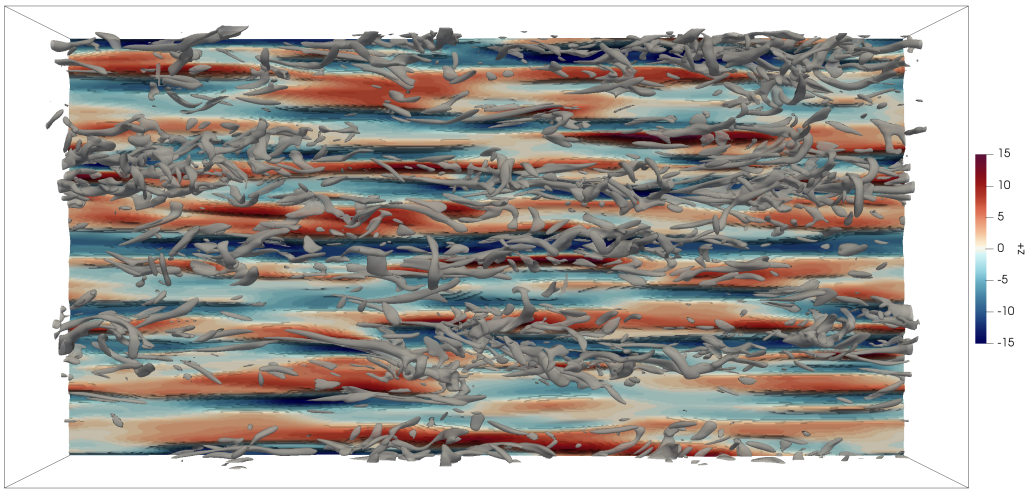

(b) $tU_b/h = 504$.

Figure 4.5: *Instantaneous wall deformation and coherent structures; flow moves from left to right.*

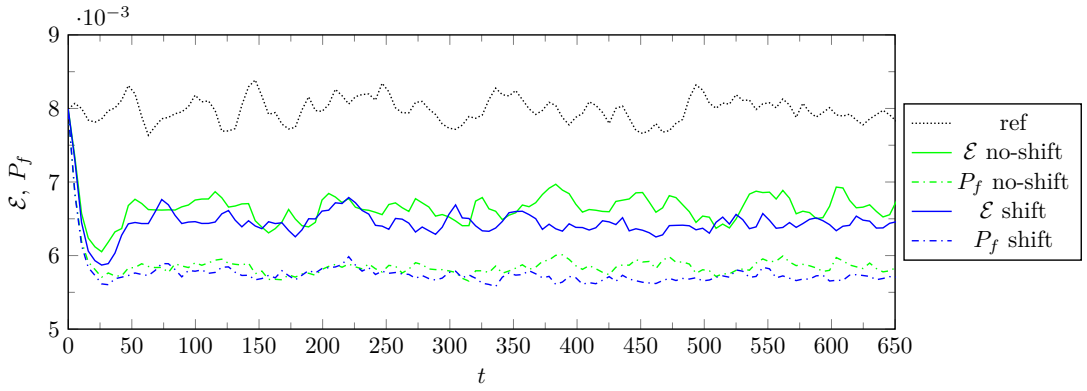

Figure 4.6: *Time trace of the total dissipation $\mathcal{E}$ and the skin friction contribution P_f.*

respect to the few known results obtained using the opposition control realized through wall deformation, instead.

4.2.2 Root-mean-square of wall displacement and velocity

Table 4.4: *Time averaged rms values of z^w and w^w non-dimensionalized with the uncontrolled skin-friction velocity u_τ.*

Case	$z^{+,w}_{rms}$	$w^{+,w}_{rms}$
no-shift	5.55	0.56
shift	5.45	0.51

In table 4.4 are reported the time-averaged root-mean-square values, normalized through the uncontrolled wall-shear velocity, of wall deformation and wall velocity. The rms value of wall deformation could be considered reasonably small if compared with the channel half-height; however, it is not so small to assume any more the channel as "hydraulically smooth" [39]. It is not clear yet in what manner and in which dimension this sort of wall roughness, caused by the control scheme, affects the near-wall flow behavior; undoubtedly, this could be a cause of the limited drag reduction rate achieved, not so much because of the form drag, but rather because this could destabilize the flow, increasing velocity fluctuations. Supplementary analysis, restricting the maximum wall deformation, should be performed to investigate whether a higher net power saving rate can be achieved. The root-mean-square value of the wall displacement is more than five times that obtained by Endo et al. [9]; however, they used a fairly greater coefficient for the integral term to suppress excessive wall deformation. Kang and Choi limited the maximum wall displacement to $z^{+,w}_{max} = 5$ [19], instead. The rms value of the wall velocity, instead, is comparable with that of the velocity fluctuation at $z^+ \simeq 30$ where the sensing plane is located, as can be deduced from figure 4.7. This suggests that the wall velocity is, as wanted, mainly due to the proportional term, which depend directly on the velocity fluctuations, rather than the integral term which, conversely, depend on the instantaneous wall deformation.

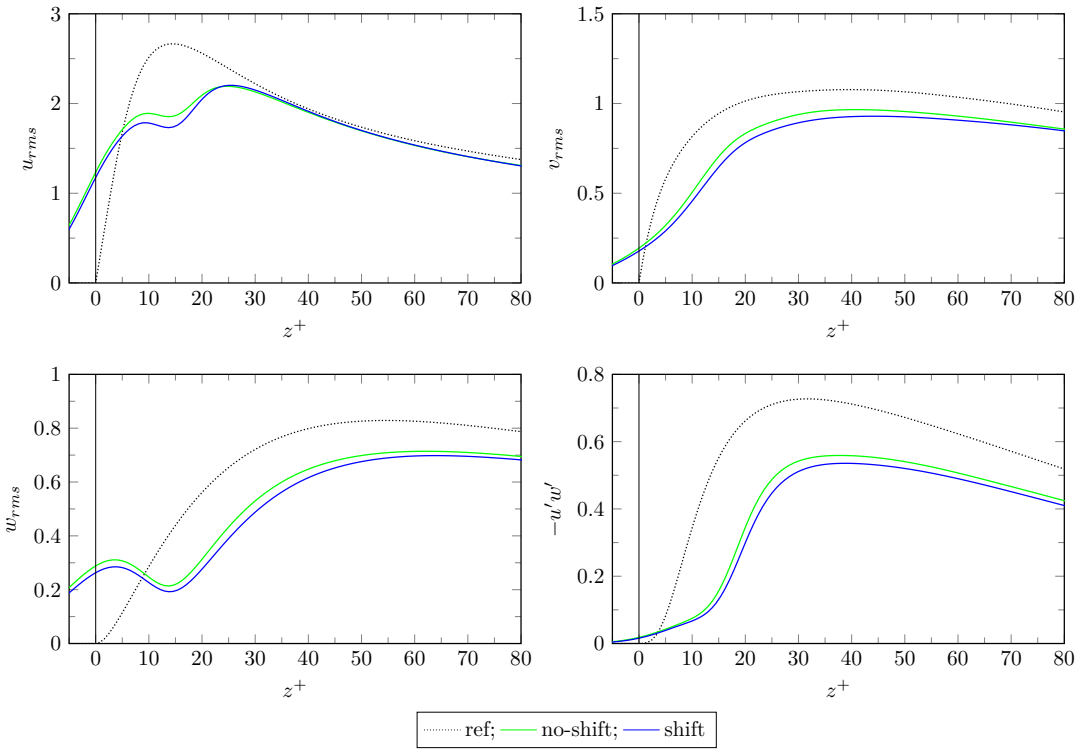

Figure 4.7: *Velocity fluctuation and Reynolds shear stress profiles. No-control skin-friction velocity is used for non-dimensionalization.*

4.2.3 Turbulence statistics

Since the wall has a highly irregular shape, a unique definition of a mean flow field is extremely tricky to be given. Undoubtedly, far from the mean wall position, all physical quantities should be insensitive to which definition is adopted. However, to better analyze the near-wall region two distinct conventions are employed in this work.

The first is straightforward: for each plane, of coordinate z, the flow variables of interest, as, for example, the streamwise flow velocity rather than the production of turbulent kinetic energy or the Reynolds shear stress, are averaged neglecting the real wall position. Subsequently, the so averaged in space physical quantities are further averaged over time. This makes sense as the root-mean-square of the wall deformation is of the order of $z^+ \simeq 5$, which is a relatively low value, and the mean wall position remains unchanged. Figure 4.7 reports the velocity fluctuation profiles and that of the Reynolds shear stress, non-dimensionalized using the uncontrolled wall-shear velocity, between $z^+ = -5$, which value is approximately equal with the root-mean-square of wall deformation, and $z^+ = 80$. All three components and the Reynolds stresses are globally reduced by the control. Unlike in the plane reference case, at $z^+ = 0$ the velocity fluctuations, as well the Reynolds shear stress, are different from 0 because of the presence of the grooves generated on the wall surface by the ejection control: even if the mean wall position is unchanged to its reference position it is also true that at $z^+ = 0$ there are certainly some points in the fluid domain. Furthermore, the use of this specific definition alters the mean quantities value also in the zone very close to the mean wall position ($z^+ < 5$). However, doing so, it is possible to separately analyze the areas of

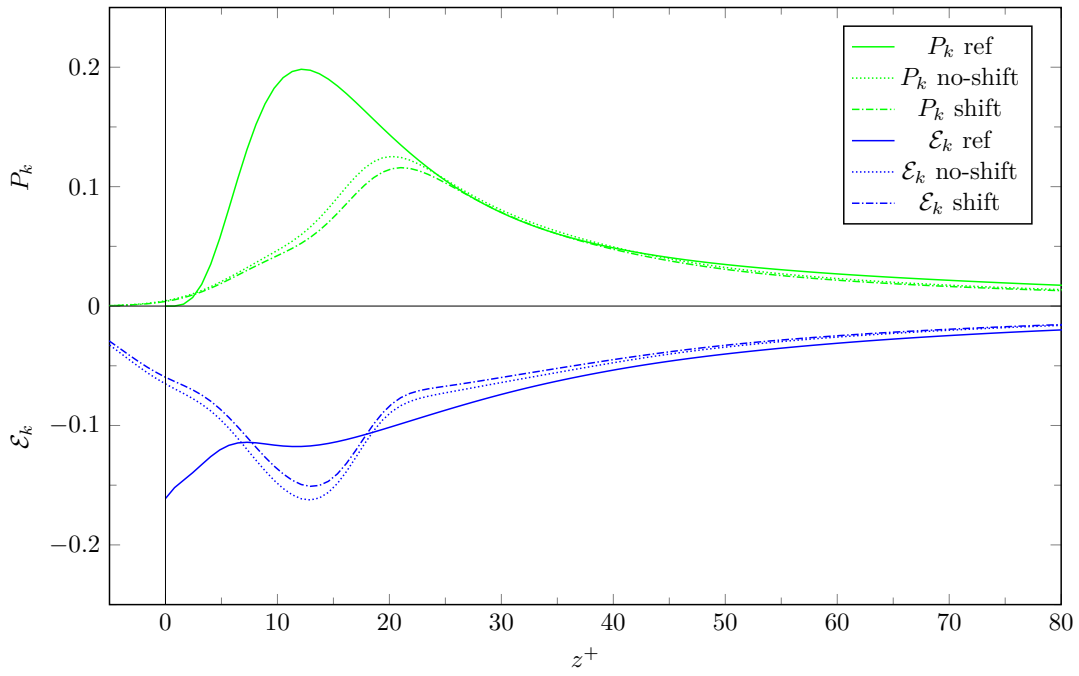

Figure 4.8: *Production (P_k) and dissipation ($\mathcal{E}_k$) of turbulent kinetic energy.*

the channel subjected to the sweep control, which lifts the wall toward the centerline, and those affected by the ejection control, which, on the contrary, pushes the wall in the opposite direction. The streamwise velocity fluctuations are substantially unchanged in the outer region ($z^+ > 40$); differently, these are significantly reduced for $10 < z^+ < 30$. Velocity fluctuation in z-direction, w_{rms}, presents a local minimum placed halfway between the mean wall position and the detection plane; in correspondence of this minimum for w_{rms} also the streamwise velocity fluctuations, u_{rms}, are slightly reduced. An almost identical behavior was found by Chung and Talha for the classical opposition control [7]. The flow control scheme lowers the Reynolds shear stress through the channel as well.

As shown in figure 4.8, the production and dissipation of the turbulent kinetic energy prove that the overall turbulence activity is weakened by the control. In particular, very close to the wall and, in the farrows dug by the ejection events control, the production of turbulent kinetic energy is practically zero: for $z^+ < 5$, $P_k/\mathcal{E}_k < 0.2$. Hence, it is possible to state that these are essentially dissipative regions. It is rather interesting to mention that if the production of turbulent kinetic is non-dimensionalized with the corrected wall-shear velocity, its peak shifts from $z^+ \simeq 12$ to $z^+ \simeq 17$, which is the same value found by Choi, Moin, and Kim for blowing/suction [6]. A peak of dissipation is found at $z^+ \simeq 15$ which is halfway between the mean wall position and the sensing plane. The maximum of the ratio between the production and the dissipation of the turbulent kinetic energy ($P_k/\mathcal{E}_k$) is likewise moved outward: with active control, it is placed at $z^+ \simeq 25$. Turbulence production, dissipation, transport, and diffusion (the latter two are not shown to have a clear view) are profoundly modified by the control scheme in the near-wall region. The outer wall region, $z^+ > 40$, is not affected by wall deformation, instead.

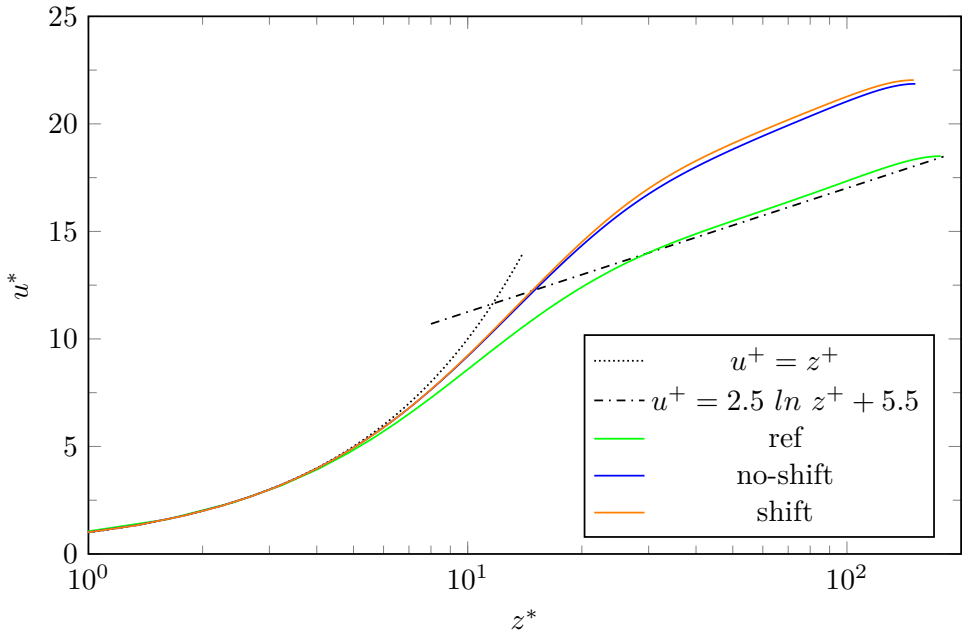

Figure 4.9: *Mean velocity profiles; u^* and z^* are made dimensionless using the actual wall-shear velocity u^*_τ.*

Another possibility to define the mean flow field is that of interpolating the flow field variables to take into account the exact distance from the solid boundary. To do that it is necessary to define a vector containing a certain number of points expressed as a function of the distance from the wall surface; then, for each point (x, y), knowing the position of the wall in that point which is saved in a file, it is required to interpolate the flow variables $(u,\ v,\ w,\ p)$ which are known in the grid nodes, instead.

The mean velocity profiles, normalized by the actual wall-shear velocities u^*_τ, and obtained from the interpolated mean flow field to take into account the local distance from the wall surface, are shown in figure 4.9. The mean velocity profiles in the simulation in which is used the upstream sensor and in that placing the actuation point precisely below the sensing point are nearly the same. The slope of the log-law in the controlled cases remains about the same as that in the reference channel. However, the logarithmic region is shifted upward: the intercept of the log low is increased from $B = 5.5$ to $B \simeq 9$. This upward shift in the log-law has been widely observed in drag-reduced flows subjected to both passive and active control techniques and could be considered a result of the increase of the viscous sublayer thickness [6].

Subsequently, the root-mean-square velocity fluctuations, the Reynolds shear stress, and the balance between the production and the dissipation of the turbulent kinetic energy have been newly calculated according to the definition, here discussed, of the mean flow field. In the near-wall region, the behavior of these quantities appears to be quite different from that obtained with the previously explained definition, apparently leading to contradictory conclusions. Adopting this second definition the rms velocity fluctuations, except for w_{rms}, and the Reynolds shear stress are correctly null when $z^+ = 0$ since this implies now zero distance from the wall surface. Conversely, in the controlled cases, w_{rms} has a non-null value at the solid boundary because of the defor-

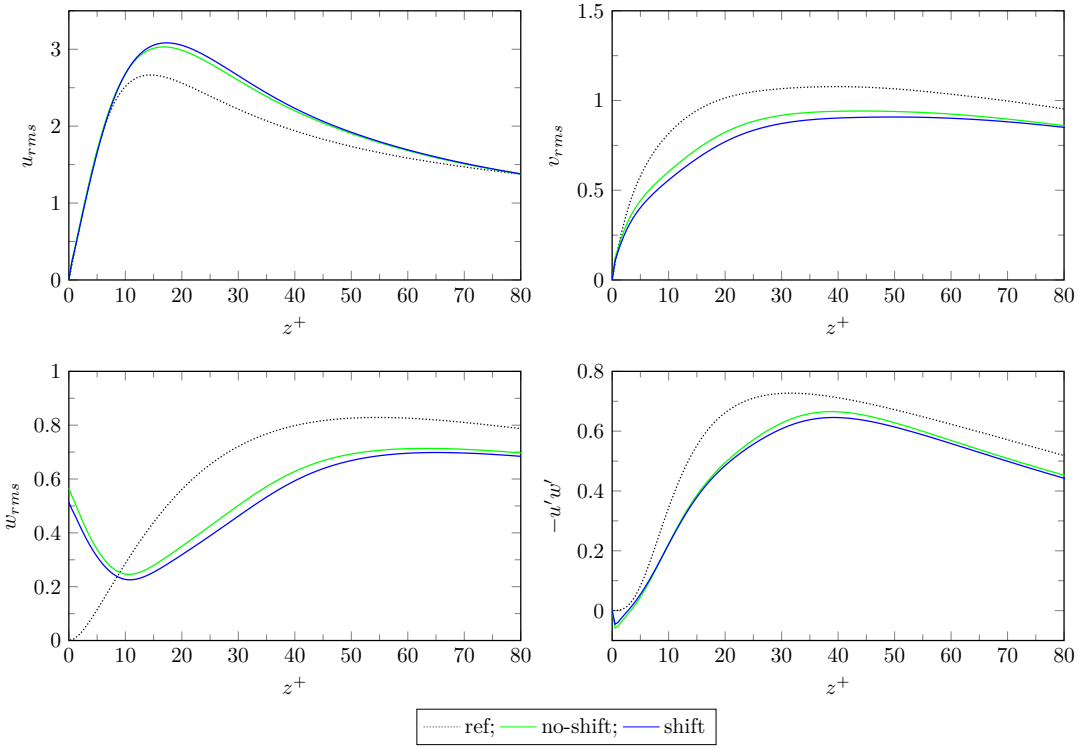

Figure 4.10: *Profile of Reynolds stresses normalized by the unmanipulated skin friction velocity.*

mation movement of the wall, which could be considered itself a fluctuating quantity. The behavior of the spanwise velocity fluctuations is essentially the same as that of the uncontrolled flow except for the amplitude reduction. Similarly, the Reynolds shear stress exhibits the same trend of the non-manipulated channel except in the viscous sublayer ($z^+ < 5$), where it is found to be negative. That latter fact is reflected in the production of turbulent kinetic energy that is likewise negative in the viscous sublayer. The skin friction coefficient in a fully developed turbulent channel flow can be written as the sum of two contributions:

- the first is a laminar skin friction contribution;
- the second is a contribution that is exclusively due to turbulence being a weighted average of the mean Reynolds shear stress in the channel.

This particular decomposition, obtained by applying a successive triple integration to the incompressible Reynolds-averaged Navier-Stokes equations, is better known as the Fukagata-Iwamoto-Kasagi (FIK) identity and its derivation can be found in [11]. The formula reads as follows:

$$C_f = \frac{6}{Re_b} + 6 \int_0^h (1 - z)(-\overline{u'w'})dz \tag{4.2}$$

Occurrences having a locally negative Reynolds shear stress have an undeniable favorable effect in reducing the skin friction drag coefficient, especially if they take place in

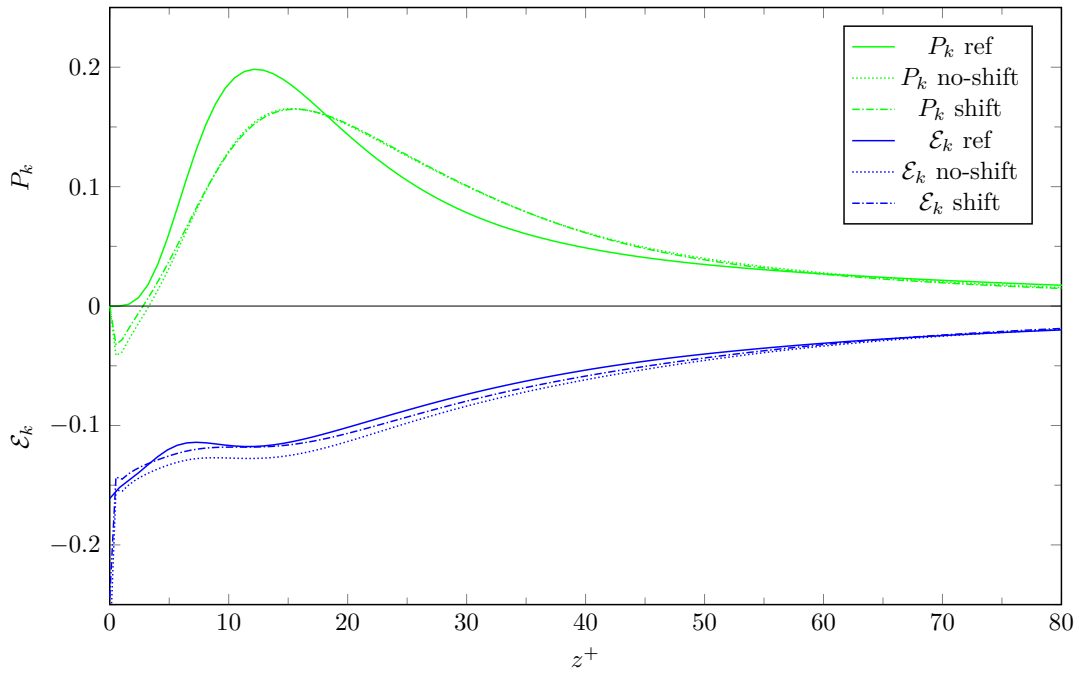

Figure 4.11: *Production (P_k) and dissipation ($\mathcal{E}_k$) of turbulent kinetic energy.*

the near-wall region, as happens in these cases (see figure 4.10). A negative Reynolds shear stress, in the near-wall region, was also observed in [31] adopting streamwise-traveling waves of wall deformation. Of particular interest is the fact that the profile of the streamwise velocity fluctuations highlights a completely different behavior. As shown in figure 4.10, the value of u_{rms} is increased for $10 < z^+ < 80$. It is known that sweep control is likely to increase the velocity fluctuation and to reduce the skin-friction, whereas the ejection control has nearly the opposite effect. Furthermore, in the grooves, the velocity is generally lower than the mean velocity; on the contrary, in the regions where the wall raised as a consequence of the sweep control, the velocity is normally higher than the mean. The combination of these two factors could explain the reason why the root-mean-square value of the streamwise velocity is increased, and this latter fact should not overly surprise. The pattern of dissipation is nearly the same as that of the reference plane channel. Nevertheless, extremely close to the wall, there is a sudden increase in the dissipation of turbulent kinetic energy: $\mathcal{E}_k = -0.24$ at $z^+ = 0$. Unluckily, the mesh resolution is not suitably high to better capture this abrupt variation in the trend of the dissipation.

CHAPTER 5

Summary and future developments

Inspired by opposition control [6], an active control law, based on a proportional-integral-differential (PID) controller, was developed with the aim of a net power saving exploiting wall deformation. Many numerical experiments have been performed using direct numerical simulation (DNS) of a fully turbulent channel flow at $Re_\tau = 180$. In particular, the grid was not body fitted, but an immersed boundary method, with a fixed Cartesian mesh, has been used. Thereby, the grid generation was trivial and was done once for all at the beginning of each simulation. Given that at the statistical steady state the total dissipation equals the sum of the pumping power and the required power for wall deformation, the net power saving rate was estimated in terms of the change in the total dissipation in a flow with a fixed mass flow rate. The wall deformation velocity was given by three terms:

- the first was opposite, through a proportionality coefficient, to the fluid z-component of the velocity at a prescribed z-location;
- the second penalized the actual wall position respect to its reference position;
- the third, eventually, damped excessive wall oscillations.

Additionally, the placement of the sensing point upstream of the actuation point has been investigated as well as selective control of sweep and ejection events.

A net power saving was obtained in almost every numerical experiment performed, proving the extended effectiveness of the control scheme. The pressure contribution was found to be negligible ($P_p \simeq \mathcal{E}/60$), which entails that even the form drag caused by the wall shape was irrelevant. The input power required for wall deformation was of the order of 10% of the total dissipation in the flow instead. Approximately $10 - 20\%$ reduction in the net power required was achieved. This value is slightly below that obtained with suction and blowing on the wall ($20 - 30\%$) but this flow control strategy

is, at the same time, more troublesome to be accomplished in real-world applications. Even some concepts explored in the present work are physically impossible to be realized. It is, in fact, inconceivable placing sensors in the middle of the flow. However, some physical quantities strongly correlated with the velocity fluctuations are already known in the literature. A continuation of the present work should investigate what can be achieved in terms of power-saving using sensors placed on the wall surface. Since the present study was conducted at a low Reynolds number, it will be additionally required to prove whether similar results could be reached even at higher Reynolds numbers. For other control strategies, such as suction and blowing, it has been demonstrated that the drag reduction decreases with increasing Reynolds numbers. However, since the present flow control strategy not only counteracts the velocity fluctuations but also modifies the inner layer flow behavior through the wall deformation, similar results should probably hold. The only way to answer this question is to conduct computations at higher Reynolds numbers than in this study.

The statistics of the manipulated channel have been compared to those of the reference plane channel flow. The control scheme intensely modified the flow behavior in the near-wall region. Velocity fluctuations and turbulence intensity were significantly reduced throughout the channel. The wall deformation was proven to be much elongated in the streamwise direction in correspondence to the quasi-streamwise vortices; this shape was demonstrated to be long-lasting in time. It is highly probable that the coherent turbulent structures and the wall shapes mutually affected one another. For this reason, a control law exploiting a time-dependent integral factor able to reduce these elongated grooves on the wall could be more effective. Other analyses, limiting the maximum wall deformation, should be performed to investigate the effect of the wall shape on the drag reduction achieved. At the same time, other active control laws, capable of detecting and counteracting the entire vortical structures, such as a controller based on the y-component of the vorticity, could be developed to increase the net power saving rate. Given the complexity of the control law, a more extensive and efficient parametric analysis, searching the best combination of the coefficients of the control scheme, could be performed using a genetic algorithm and imposing the net power saving rate as the fitness function.

For all these reasons, this work can be deemed a valued starting point providing many new possibilities.

Bibliography

[1] Asai M., Konishi Y., Oizumi Y., Nishioka M. Growth and breakdown of low-speed streaks leading to wall turbulence. *Journal of Fluid Mechanics*, 586:371–396, 2007.

[2] Aström K. J., Hägglund T. *PID Controllers: Theory, Design, and Tuning, Second Edition*. International Society of Automation, 1995.

[3] Banchetti J., Luchini P., Quadrio M. Turbulent drag reduction over curved walls. *Journal of Fluid Mechanics*, 896(A10), 2007.

[4] Bolzern P., Scattolini R., Schiavoni N. *Fondamenti di controlli automatici*. McGraw Hill, 2015.

[5] Choi H., Moin P., Kim J. Direct numerical simulation of turbulent flow over riblets. *Journal of Fluid Mechanics*, 255:503–539, 1993.

[6] Choi H., Moin P., Kim J. Active turbulence control for drag reduction in wall-bounded flows. *Journal of Fluid Mechanics*, 262:75–110, 1994.

[7] Chung M., Talha T. Effectiveness of active flow control for turbulent skin friction drag reduction. *Physics of fluid*, 23(025102), 2011.

[8] Dubief Y., Delcayre F. On coherent-vortex identification inturbulence. *Journal of turbulence*, 1(11), 2000.

[9] Endo T., Kasagi N., Suzuki Y. Feedback control of wall turbulence with wall deformation. *Heat and fluid flow*, 21:568–575, 2000.

[10] Fadlun E. A., Verzicco R., Orlandi P., Mohd-Yusof J. Combined immersed-boundary finite-differences methods for three-dimensional complex flow simulations. *Journal of Computational Physycs*, (161):35–60, 2000.

[11] Fukagata K., Iwamoto K., Kasagi N. Contribution of reynolds stress distribution to the skin friction in wall-bounded flows. *Physics of fluids*, (14):L73–L76, 2002.

[12] Fukagata K., Sugiyama K., Kasagi N. On the lower bound of net driving power incontrolled duct flows. *Physica*, D(238):1082–1086, 2009.

[13] Hamiltion J. M., Kim J., Waleffe F. Regeneration mechanisms of near-wall turbulence structures. *Journal of Fluid Mechanics*, 287:317–348, 1995.

[14] Hunt J. C. R., Wray A. A., Moin P. Eddies, stream, and convergence zones in turbulent flows. *Center for Turbulent Research Report*, CTR-S88:193–208, 1988.

[15] Iaccarino G., Verzicco R. Immersed boundary technique for turbulent flow simulations. *Appl. Mech. Reviews*, 56:331–347, 2003.

[16] Iwamoto K., Suzuki Y., Kasagi N. Reynolds number effect on wall turbulence:toward effective feedback control. *Intl J. Heat Fluid Flow*, (23):678–689, 2002.

[17] Jeong J., Hussain F., Schoppa W., Kim J. Coherent structures near the wall in a turbulent channel flow. *Journal of Fluid Mechanics*, 332:185–214, 1997.

[18] Jiménez J., Pinelli A. The autonomous cycle of near-wall turbulence. *Journal of Fluid Mechanics*, 389:335–359, 1999.

[19] Kang S., Choi H. Active wall motions for skin-friction drag reduction. *Physics of fluid*, 12(12), 2000.

[20] Kasagi N., Suzuki Y., Fukagata K. Microelectromechanical system-based feedback control of turbulence for skin friction reduction. *Annual Review of fluid mechanics*, 41:231–251, 2009.

[21] Kim H. T., Kline S. J., Reynolds W. C. The production of turbulence near a smooth wall in a turbulent boundary layer. *Journal of Fluid Mechanics*, 50:133–160, 1971.

[22] Kim J., Choi H. Linear proportional-integral control for skin-friction reduction in a turbulent channel flow. *Journal of Fluid Mechanics*, 814:430–451, 2017.

[23] Kim J., Hussain F. Propagation velocity of perturbations in turbulent channel flow. *Physics of fluid A*, 5(3):695–706, 1993.

[24] Kim J., Moin P., Moser R. Turbulence statistics in fully developed channel flow at low reynolds number. *Journal of Fluid Mechanics*, 177:133–166, 1987.

[25] Lee C., Kim J., Babcock D., Goodman R. Application of neural networks to turbulence control for drag reduction. *Physics of Fluid*, 9(6):1740–1747, 1997.

[26] Lee C., Kim J., Choi H. Suboptimal control of turbulent channel flow for drag reduction. *Journal of Fluid Mechanics*, 358:245–258, 1998.

[27] Lee J. Opposition control of turbulent wall-bounded flow using upstream sensor. *Journal of mechanical science and technology*, 29(11):4729–4735, 2015.

[28] Lee K. H., Cortelezzi L., Kim J., Speyer J. Application of reduced-order controller to turbulent flows for drag reduction. *Physics of Fluid*, 13(5):1321–1330, 2001.

[29] Luchini P. Immersed-boundary simulation of turbulent flow past a sinusoidally undulated river bottom. *Eur. J. Mech. B / Fluids*, 55:340–347, 2016.

[30] Mansour N. N., Kim J., Moin P. Reynolds-stress and dissipation-rate budgets in a turbulent channel flow. *Journal of Fluid Mechanics*, 194:15–44, 1988.

[31] Nakanishi R., Mamori H., Fukagata K. Relaminarization of turbulent channel flow using traveling wave-like deformation. *International journal of heat and fluid flow*, 35:152–159, 2012.

[32] Nguyen C. T. Mems technology for timing and frequency control. *IEEE Transactions on Ultrasonics, Ferroelectrics, and Frequency Control*, 54(2):251–270, 2007.

[33] Orlandi P., Leonardi S. Dns of turbulent channel flow with two- and three-dimensional roughness. *Journal of Turbulence*, 7(53), 2006.

[34] Pamiés M., Garnier E., Merlen A., Sagaut P. Response of a spatially daveloping turbulent boundary layer to active controlnstrategies in the framework of opposition control. *Physics of fluids*, 19(108102), 2007.

[35] Pantom R. L. Overview of the self-sustaining mechanism of wall turbulence. *Prog. Aerosp. Sci.*, 37:341–383, 2001.

[36] Pope S. B. *Turbulent Flows*. Cambridge University Press, 2000.

[37] Quadrio M., Ricco P. Critical assessment of turbulent drag reductionthrough spanwise wall oscillations. *Journal of Fluid Mechanics*, 521:251–271, 2004.

[38] Robinson S. K. Coherent motions in the turbulent boundary layer. *Annual review of fluid mechanics*, 23:601–639, 1991.

[39] Schlichting H. *Boundary layer theory*. Springer, 1960.

[40] Francesco Secchi. Immersed boundary simulation of turbulent flow through a peristaltic actuator, 2017-2018.

[41] Son D., Jeon S., Choi H. A proportional-integral-differential control of flow over a circular cylinder. *Phil. Trans. R. Soc A*, 369:1540–1555, 2011.

[42] Walsh M. J. Riblets as a viscous drag reduction technique. *AIAA journal*, 21(4):485–486, 1983.

[43] Zhang Y., Wang X., Liu C. Comparisons of and analyses of vortex identification between omega method and q criterion. *Journal of Hydrodynamics*, 31(1), 2019.

[44] Zhou J., Adrian R. J., Balachandar S., Kendall T. M. Mechanism for generating coherent packets of hairpin vortices in channel flow. *Journal of Fluid Mechanics*, 387:353–396, 1999.